Electrophysiological characterization and computational models of HVC neurons in the zebra finch

Arij Daou, Matthew T. Ross, Frank Johnson, Richard L. Hyson and Richard Bertram

J Neurophysiol 110:1227-1245, 2013. First published 29 May 2013;
doi: 10.1152/jn.00162.2013

You might find this additional info useful...

This article cites 78 articles, 42 of which you can access for free at:
http://jn.physiology.org/content/110/5/1227.full#ref-list-1

Updated information and services including high resolution figures, can be found at:
http://jn.physiology.org/content/110/5/1227.full

Additional material and information about ***Journal of Neurophysiology*** can be found at:
http://www.the-aps.org/publications/jn

This information is current as of September 3, 2013.

Journal of Neurophysiology publishes original articles on the function of the nervous system. It is published 24 times a year (twice monthly) by the American Physiological Society, 9650 Rockville Pike, Bethesda MD 20814-3991. Copyright © 2013 the American Physiological Society. ESSN: 1522-1598. Visit our website at http://www.the-aps.org/.

Downloaded from http://jn.physiology.org/ at Florida State University on September 3, 2013

J Neurophysiol 110: 1227–1245, 2013.
First published May 29, 2013; doi:10.1152/jn.00162.2013.

Electrophysiological characterization and computational models of HVC neurons in the zebra finch

Arij Daou,[1] Matthew T. Ross,[2] Frank Johnson,[2,3] Richard L. Hyson,[2,3] and Richard Bertram[1,2]
[1]*Department of Mathematics, Florida State University, Tallahassee, Florida;* [2]*Program in Neuroscience, Florida State University, Tallahassee, Florida; and* [3]*Department of Psychology, Florida State University, Tallahassee, Florida*

Submitted 5 March 2013; accepted in final form 24 May 2013

Daou A, Ross MT, Johnson F, Hyson RL, Bertram R. Electrophysiological characterization and computational models of HVC neurons in the zebra finch. *J Neurophysiol* 110: 1227–1245, 2013. First published May 29 2013; doi:10.1152/jn.00162.2013.—The nucleus HVC (proper name) within the avian analog of mammal premotor cortex produces stereotyped instructions through the motor pathway leading to precise, learned vocalization by songbirds. Electrophysiological characterization of component HVC neurons is an important requirement in building a model to understand HVC function. The HVC contains three neural populations: neurons that project to the RA (robust nucleus of arcopallium), neurons that project to Area X (of the avian basal ganglia), and interneurons. These three populations are interconnected with specific patterns of excitatory and inhibitory connectivity, and they fire with characteristic patterns both in vivo and in vitro. We performed whole cell current-clamp recordings on HVC neurons within brain slices to examine their intrinsic firing properties and determine which ionic currents are responsible for their characteristic firing patterns. We also developed conductance-based models for the different neurons and calibrated the models using data from our brain slice work. These models were then used to generate predictions about the makeup of the ionic currents that are responsible for the different responses to stimuli. These predictions were then tested and verified in the slice using pharmacological manipulations. The model and the slice work highlight roles of a hyperpolarization-activated inward current (I_h), a low-threshold T-type Ca^{2+} current ($I_{Ca\text{-}T}$), an A-type K^+ current (I_A), a Ca^{2+}-activated K^+ current (I_{SK}), and a Na^+-dependent K^+ current (I_{KNa}) in driving the characteristic neural patterns observed in the three HVC neuronal populations. The result is an improved characterization of the HVC neurons responsible for song production in the songbird.

birdsong; computational model; ionic currents; song system

ZEBRA FINCHES ARE EXTRAORDINARY VOCALISTS within the oscine family of songbirds that, like humans, learn to produce highly stereotyped complex sequences of vocal gestures (Bolhuis and Gahr 2006; Bolhuis et al. 2010; Bottjer and Arnold 1997; Brainard and Doupe 2000, 2002; Doupe et al. 2005; Fee and Scharff 2010; Margoliash 2010; Margoliash and Schmidt 2010; Mooney 2009; Simonyan et al. 2012; Williams 2004). The acquisition and production of birdsong occurs through a set of forebrain nuclei that form a well-characterized network (Fig. 1), known as the "song system" (Bolhuis et al. 2010; Margoliash 2010; Margoliash and Schmidt 2010; Nottebohm 2005). Nucleus HVC plays a key role in the song system. Neurons in the HVC serve the role of the conductor of the song, having a pattern-generating role coding for syllable order and controlling the overall temporal structure of birdsong (Fee and Goldberg 2011; Fee et al. 2004; Fee and Scharff 2010; Long and Fee 2008; Mooney 2009; Mooney and Spiro 1997; Vu et al. 1994; Yu and Margoliash 1996).

Precisely how neurons in HVC encode song sequence and phonology is poorly understood. Models of how neurons might be organized and interconnected have been proposed (Abarbanel et al. 2004a, 2004b; Drew and Abbott 2003; Gibb et al. 2009a, 2009b; Jin 2009; Jin et al. 2007; Katahira et al. 2007; Li and Greenside 2006; Long et al. 2010; Mooney and Prather 2005; Troyer and Doupe 2000), and techniques for calibrating HVC models are being developed (Abarbanel et al. 2012), but a complete biophysical model is limited by the lack of detailed understanding of the properties of the component neurons. A goal of the present series of experiments is to detail the biophysical properties of cell types in HVC. There are three neuronal populations in the zebra finch HVC (Kubota and Taniguchi 1998; Mooney 2000; Mooney and Prather 2005): neurons that project to the robust nucleus of arcopallium (RA; HVC_{RA} neurons), neurons that project to Area X (HVC_X neurons), and interneurons (HVC_{INT} neurons). The three types of HVC neurons have different functional and cellular properties that may be important for the different functions performed by the neural circuits within the HVC and for communication with the rest of the song system.

Numerous in vivo and in vitro intracellular recording studies of HVC neurons have been carried out (Dutar et al. 1998; Katz and Gurney 1981; Kubota and Saito 1991; Kubota and Taniguchi 1998; Lewicki 1996; Lewicki and Konishi 1995; Long et al. 2010; Mooney 2000; Mooney et al. 2001; Mooney and Prather 2005; Schmidt and Perkel 1998; Shea et al. 2010; Solis and Perkel 2005; Wild et al. 2005). These studies shed light on several neuronal and circuit mechanisms and unveiled a variety of physiological properties within the HVC. For example, the brain slice studies demonstrated that HVC_{RA}, HVC_X, and HVC_{INT} neurons have distinct, categorical electrophysiological phenotypes (Dutar et al. 1998; Kubota and Saito 1991; Kubota and Taniguchi 1998; Mooney 2000; Mooney et al. 2001; Mooney and Prather 2005; Shea et al. 2010; Wild et al. 2005).

The studies published thus far have characterized HVC neurons according to their responses to injected current. HVC_X neurons exhibit fast and time-dependent inward rectification where a sag appears in response to hyperpolarizing current pulses. In addition, HVC_X neurons exhibit spike frequency adaptation (accommodation) in response to injected depolarizing currents. HVC_{RA} neurons, on the other hand, have a more negative resting membrane potential than the other classes and do not exhibit a sag in response to hyperpolarizing current pulses. The RA-projecting neurons also fire with one or few

---

Address for reprint requests and other correspondence: R. Bertram, Dept. of Mathematics and Program in Neuroscience, Florida State Univ., Tallahassee, FL 32306-4301 (e-mail: bertram@neuro.fsu.edu).

0022-3077/13 Copyright © 2013 the American Physiological Society

Downloaded from http://jn.physiology.org/ at Florida State University on September 3, 2013

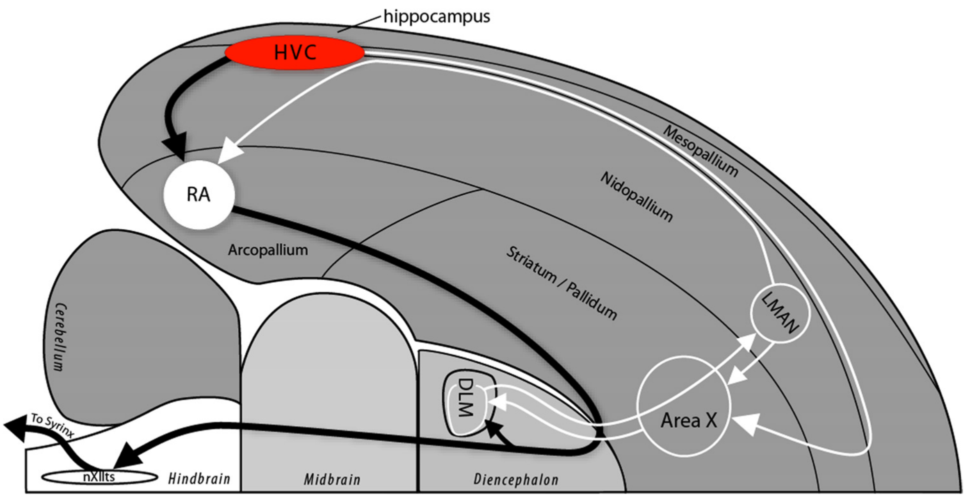

Fig. 1. Sagittal perspective schematic of an adult male zebra finch brain shows the position of HVC in the dorsocaudal nidopallium. The hippocampus is positioned above pallial structures in birds. DLM, medial dorsolateral nucleus of the thalamus; LMAN, lateral portion of the magnocellular nucleus of the anterior neostriatum; nXIIts, brain stem nucleus XII (tracheosyringeal part); RA, robust nucleus of arcopallium.

action potentials in response to a relatively large depolarizing pulse, often with a delay. Finally, HVC interneurons exhibit a more prominent sag than HVC_X neurons and produce rebound firing following hyperpolarizing current pulses. In response to depolarizing pulses, HVC_{INT} neurons fire tonically with high firing frequency and with little or no adaptation. Despite the electrical identification of HVC neurons, the ionic currents underlying these behaviors in the different HVC neuron types remain largely unexamined and unknown.

In this study, we obtained whole cell current-clamp recordings from neurons within the HVC to determine which ionic currents are responsible for their characteristic firing patterns. We also developed conductance-based models for the different neurons based on the identified ionic currents and their reported characteristics and then calibrated the models using data from our brain slice work. These models were then used to generate predictions about the frequency-response curve and the effects of blocking selected currents. Model predictions were then tested and verified in the slice using various pharmacological manipulations. The result is an improved characterization of the HVC neurons responsible for singing in the songbird.

MATERIALS AND METHODS

Brain Slice Electrophysiology

Slice preparation. Adult male zebra finches (n = 34, >120 days after hatch) raised in our breeding colony at Florida State University (FSU) were used for experiments. Animal care and experiments were performed in accordance with National Science Foundation guidelines and approved by the FSU Animal Care and Use Committee. Birds were anesthetized with isoflurane and rapidly decapitated. The brain was quickly removed and placed in ice-cold artificial cerebrospinal fluid (ACSF) that was pregassed with 95% O_2-5% CO_2. The hippocampus of each hemisphere was then resected over the general area of one side of the posterior lobe. This allowed us to clearly visualize HVC as an oval-like extrusion of the cerebrum, which allowed for accurate sectioning (Fig. 2*A*). Next, the brain was cut midsagittally to separate the hemispheres. Each hemisphere was glued to a custom stage of a vibrating microtome immersed in ice-cold ACSF, and 175- to 300-μm parahorizontal slices were prepared. The ACSF used for slice preparation had equimolar sucrose partially replacing NaCl (Aghajanian and Rasmussen 1989) and contained (in mM) 72 sucrose, 83 NaCl, 3.3 $MgCl_2$, 0.5 $CaCl_2$, 1.0 NaH_2PO_4, 26.2 $NaHCO_3$, and 22 glucose (osmolarity 285–295 mosM). Slices were incubated for 15 min in the same sucrose ACSF solution at room temperature, followed by further incubation (45 min or more) in standard NaCl recording solution (with no sucrose), which contained (in mM) 119 NaCl, 2.5 KCl, 1.3 $MgCl_2$, 2.5 $CaCl_2$, 1.0 NaH_2PO_4, 26.2 $NaHCO_3$, and 22 glucose (osmolarity 285–295 mosM).

Whole cell recording. Recordings were initiated after 1 h of total incubation. One slice at a time was transferred to a submersion chamber where it was superfused with pregassed standard NaCl ACSF. The HVC was initially identified as a dark region in the slice (due to the heavy myelination of HVC) through a light microscope when transilluminated from below (Fig. 2*A*). Whole cell patch-clamp recordings from HVC neurons were made with unpolished electrodes (4–9 MΩ). All electrodes were pulled with a Sutter Instruments (Novato, CA) P-80 micropipette puller. The electrodes were filled with the following intracellular solution (in mM): 100 K-gluconate, 5 $MgCl_2$, 10 EGTA, 2 Na_2-ATP, 0.3 Na_3-GTP, and 40 HEPES, pH adjusted to 7.2–7.3 with KOH. A modified pipette solution was used during some experiments consisting of (in mM) 125 K-gluconate, 15 KCl, 1 $MgCl_2$, 10 HEPES, 0.2 EGTA, 2 Mg-ATP, and 0.3 Na_3-GTP. No differences in recordings were observed between these solutions. Electrodes were injected with positive pressure and advanced through the slice until apposition to HVC neurons was clearly visualized (Fig. 2*C*). HVC cells were then slowly approached until the pipette resistance increased. Negative pressure was then applied until a gigaohm seal was obtained, and the patch membrane was ruptured by further application of negative pressure. Only cells that showed a stable membrane potential below −55 mV and that spiked readily in response to positive current injection were considered for further analysis. Voltage traces were corrected for an empirically measured liquid junction potential (+6 mV for standard ACSF and pipette solutions). Whole cell recordings of the membrane potential were made using a Multiclamp 700B (Axon Instruments, Foster City, CA), with an active bridge circuit for passing current, and digitized (Digidata 1322A; Axon Instruments) while connected to a personal computer running Axon pClamp 9 acquisition software (Molecular Devices, Sunnyvale, CA).

Pharmacological manipulations. Pharmacological tests used various drugs, which were delivered by bath application at the following concentrations: 6-cyano-7-nitroquinoxaline-2,3-dione (CNQX, 5 and 10 μM; no. 0190, Tocris), picrotoxin (PTX, 50 μM; no. 1128, Tocris), ZD 7288 (30 and 50 μM; no. 1000, Tocris), 4-aminopyridine (4-AP, 0.3 mM; no. 0940, Tocris), apamin (150 nM; no. A1289, Sigma), mibefradil (6 μM; no. 2198, Tocris), and quinidine (100 μM; no. 4108, Tocris). The drugs CNQX, picrotoxin, and quinidine were dissolved in DMSO (final concentration 0.1%), whereas ZD 7288, 4-AP, and mibefradil were dissolved in water, and apamin was

Downloaded from http://jn.physiology.org/ at Florida State University on September 3, 2013

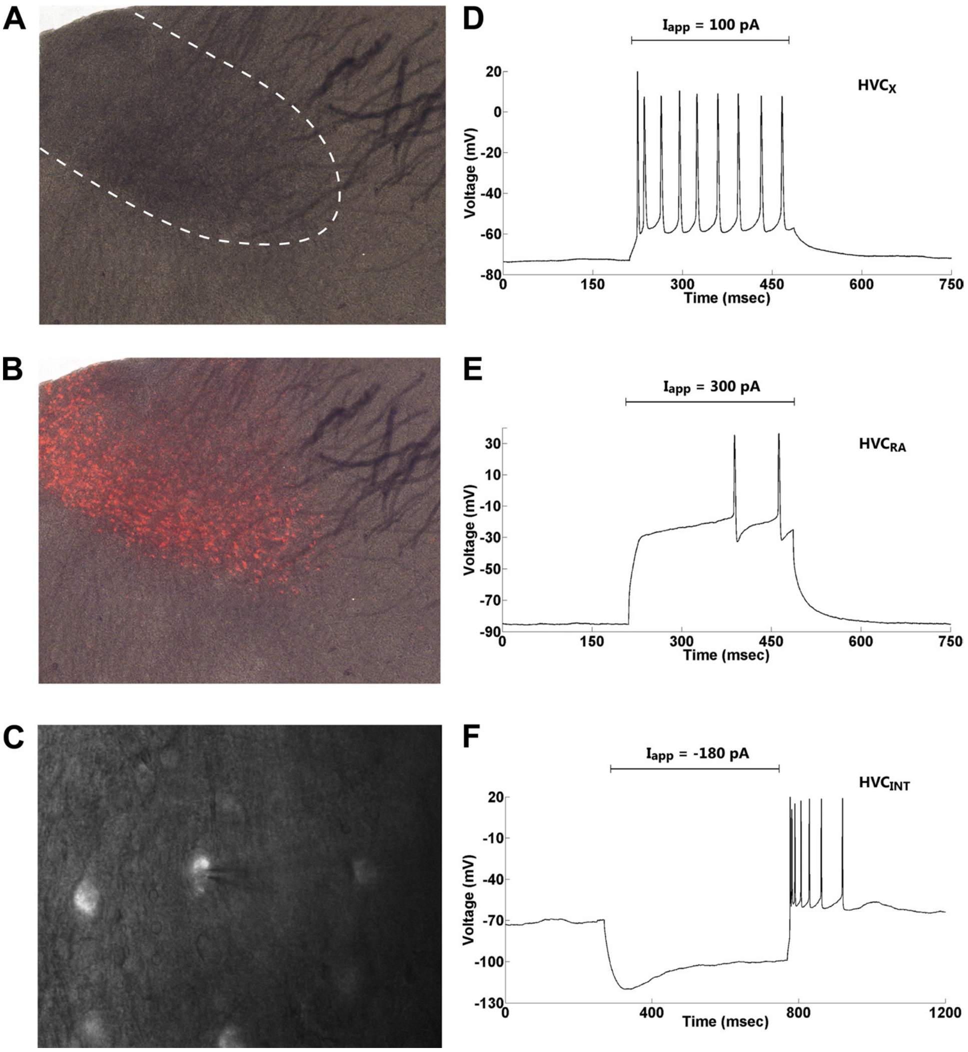

Fig. 2. Anatomic confirmation of physiological classification. *A*: under brightfield illumination, HVC has a darkened appearance (due to heavy myelination) with striations of fibers (dashed white line highlights HVC region). *B*: focal infusions of DiI into Area X in vivo, retrogradely labeling X-projecting (HVC_X) neurons that could be readily observed in the slice preparation under epifluorescence illumination. Composite of the brightfield (*A*) and fluorescent images shows HVC_X neurons throughout the HVC. *C*: an electrode patched onto a fluorescently labeled HVC_X neuron (composite of the brightfield and fluorescent illumination). *D*: recording from the labeled neuron in *C* showing a firing pattern that is characteristic of HVC_X neurons ($n = 5$). *E*: recording from an RA-projecting (HVC_{RA}) neuron that was labeled using similar methods shows its characteristic properties ($n = 2$). *F*: recording from a neuron that was not fluorescently labeled shows properties that resembles those of an HVC interneuron (HVC_{INT}).

dissolved in 0.05 M acetic acid. All drugs were aliquoted and stored at −20°C except for 4-AP, which was kept at room temperature.

Electrophysiological identification of neurons. All HVC neurons in this study were classified on the basis of their electrophysiological properties, as described previously (Dutar et al. 1998; Kubota and Saito 1991; Kubota and Taniguchi 1998; Mooney 2000; Mooney et al. 2001; Mooney and Prather 2005; Schmidt and Perkel 1998; Shea et al. 2010; Wild et al. 2005).

We applied three tests for the identification of HVC neurons online. The first test was the response obtained to depolarizing current pulses. In particular, HVC_{RA} neurons fire only one to a few action potentials in response to +200-pA currents of ~0.5-s duration, whereas HVC_X neurons fire more regularly with moderate spike frequency adaptation and HVC_{INT} neurons fire at high frequency with little or no spike frequency adaptation (Dutar et al. 1998; Kubota and Taniguchi 1998; Mooney 2000; Mooney et al. 2001; Mooney and Prather 2005; Schmidt and Perkel 1998; Shea et al. 2010; Wild et al. 2005). The second test was the voltage response to hyperpolarizing current pulses. HVC_{INT} neurons exhibit a prominent sag in response to hyperpolarizing currents, whereas HVC_X neurons exhibit a less prominent sag and HVC_{RA} neurons exhibits no sag at all (Dutar et al. 1998; Kubota and Saito 1991; Kubota and Taniguchi 1998). The final test was an examination of the resting membrane potential. HVC_{INT} neurons generally exhibit a resting membrane potential of −60 ± 6 mV, whereas HVC_X neurons exhibit a resting membrane potential of −72 ± 7 mV and HVC_{RA} neurons exhibit a resting membrane potential of −85 ± 6 mV (Dutar et al. 1998; Kubota and Taniguchi 1998).

Spike afterhyperpolarization (AHP), time to peak (TTP), sag ratio (SR), and adaptation ratio (AR) physiological measurements were also computed offline to help assess and confirm the online categorization. Spike threshold was computed as the peak of the second derivative of the voltage trace. Spike AHP and TTP were measured relative to the spike threshold point. The SR during hyperpolarization was computed as $(V_{min} - V_{end})/V_{min}$, where V_{end} represents the voltage at the end of the hyperpolarizing current pulse and V_{min} represents the voltage at the nadir (the minimum voltage). The sag was computed for hyperpolarizing pulses of duration 500 ms and magnitude −200 pA. Spike frequency adaptation was quantified by computing the AR between the last interspike interval and the first interspike interval for depolarizing current pulses of duration 500 ms and magnitude 150 pA. A ratio of 1 indicates that there is no adaptation, and larger magnitudes of AR indicate stronger adaptation.

The electrophysiological recordings were first read with Clampfit 9.0 (Axon Instruments), and the traces were saved in Axon Text File (.atf) format. The .atf data were then read with a custom Matlab (MathWorks) routine, and all further analysis was made using custom Matlab routines.

In vivo injections of retrograde tracers into Area X and RA. Physiological categorization of HVC_X and HVC_{RA} neurons was confirmed in two birds by recording from cells that were fluorescently labeled using a retrograde tracing dye that was injected into Area X or RA. The birds were deeply anesthetized with Equithesin (0.05 ml) and secured in the stereotaxic instrument, and the skull was exposed by

Downloaded from http://jn.physiology.org/ at Florida State University on September 3, 2013

making an incision down the center of the scalp and retracting the skin using curved forceps. The bifurcation at the midsagittal sinus was used as stereotaxic zero, and a small craniotomy over left and right Area X or RA was made using predetermined coordinates. Tracer (DiI; Life Technologies; ~400 nl) was then delivered into Area X (or RA) bilaterally via a glass micropipette attached to a gas pressure injection system (Applied Scientific Instrumentation MPPI-3).

After a 6-day period for tracer transport, the birds were used for brain slice electrophysiology studies. HVC neurons that were retrogradely labeled were easily identified in the recording chamber with the use of epifluorescence illumination (Fig. 2, *B* and *C*). Unlabeled neurons were also recorded to confirm that only retrogradely labeled cells display the physiological phenotype of the targeted HVC_X or HVC_RA neurons (Fig. 2*F*).

Computational Modeling

Single-compartment conductance-based biophysical models of cells from the HVC were developed, based on our current-clamp data. Simulations of these model neurons were performed using Matlab (MathWorks). The source codes containing the models are available on the FSU website (http://www.math.fsu.edu/~bertram/software/birdsong) as well as the ModelDB website (http://senselab.med.yale.edu/modeldb/).

Model HVC cells. We used Hodgkin-Huxley-type models with additional currents added to reproduce features of the voltage traces observed in our current-pulse studies. The functional forms of activation/inactivation functions and time constants were based on published neural models (Destexhe and Babloyantz 1993; Dunmyre et al. 2011; Hodgkin and Huxley 1952; Terman et al. 2002; Wang et al. 2003), and the majority of our fitting parameters were maximum conductance, which are likely to vary among cell types. The sag seen in HVC_X and HVC_INT neurons (Dutar et al. 1998; Kubota and Saito 1991; Kubota and Taniguchi 1998) suggests that a hyperpolarization-activated inward current conductance is present, and the postinhibitory rebound firing seen in these neurons suggests that a low-threshold T-type Ca^{2+} current conductance may be present. Also, the delay to spiking seen in the response of HVC_RA neurons to depolarizing pulses (Kubota and Taniguchi 1998; Mooney and Prather 2005) hints at expression of the A-type K^+ current in these neurons. Moreover, the depolarization block and plateau potential that some HVC neurons exhibit in response to positive current pulses (Kubota and Saito 1991) is an indicator of the existence of a persistent sodium current or some other long-lasting inward current. The presence of some conductances had been shown in previous studies, and in these cases they were included in our models. For example, Na^+- and Ca^{2+}-dependent K^+ conductances have been identified before (Dutar et al. 1998; Kubota and Saito 1991; Kubota and Taniguchi 1998; Schmidt and Perkel 1998), and a high-threshold Ca^{2+} conductance has been shown to exist in HVC neurons (Kubota and Saito 1991; Long et al. 2010).

With this background, the model was designed to include spike-producing currents (I_K and I_Na), a high-threshold L-type Ca^{2+} current ($I_\text{Ca-L}$), a low-threshold T-type Ca^{2+} current ($I_\text{Ca-T}$), a small-conductance Ca^{2+}-activated K^+ current (I_SK), a persistent Na^+ current (I_Nap), a Na^+-dependent K^+ current (I_KNa), an A-type K^+ current (I_A), a hyperpolarization-activated cation current (I_h), and a leak current (I_L). The membrane potential of each HVC neuron obeys the current balance equation:

$$C_\text{m}\frac{\text{d}V}{\text{d}t} = -I_\text{L} - I_\text{K} - I_\text{Na} - I_\text{Ca-L} - I_\text{Ca-T} - I_\text{A} - I_\text{SK} - I_\text{KNa} - I_\text{h} - I_\text{Nap} + I_\text{app}, \tag{1}$$

where I_app represents the constant applied current and C_m is membrane capacitance.

Ionic current equations. VOLTAGE-GATED IONIC CURRENTS. The constant-conductance leak current is $I_\text{L} = g_\text{L}(V - V_\text{L})$. The voltage-dependent currents have non-constant conductances (g) with activation/inactivation kinetics characterized as fast, instantaneous, or slow as described below. The voltage-dependent currents are

$$I_\text{K} = g_\text{K}n^4(V - V_\text{K}) \tag{2}$$

$$I_\text{Na} = g_\text{Na}m_\infty^3(V)h(V - V_\text{Na}) \tag{3}$$

$$I_\text{Nap} = g_\text{Nap}mp_\infty(V)hp(V - V_\text{Na}) \tag{4}$$

$$I_\text{A} = g_\text{A}a_\infty(V)e(V - V_\text{K}) \tag{5}$$

$$I_\text{Ca-L} = g_\text{Ca-L}Vs_\infty^2(V)\left(\frac{Ca_\text{ex}}{1 - e^{\frac{2FV}{RT}}}\right), \tag{6}$$

where

$$x_\infty(V) = \frac{1}{1 + e^{\left(\frac{V-\theta_x}{\sigma_x}\right)}}, \quad x = m,\ mp,\ a,\ \text{or } s, \tag{7}$$

and where θ_x is the half-activation (or half-inactivation) voltage for gating variable x and σ_x is the slope factor for that variable. The term *RT/F* is the thermal voltage, where *T* is the temperature of the bathing solution (25°C or 298 K), *R* is the gas constant, and *F* is Faraday's constant. Ca_ex is the external Ca^{2+} concentration, which is 2.5 mM in the bathing solution. The persistent Na^+ current is modeled as in Dunmyre et al. (2011) with instantaneous activation and slow inactivation variables. The steady-state activation functions for the fast gating variables that are treated as instantaneous are shown in Fig. 3*A* [m_∞ (black), a_∞ (blue), s_∞ (cyan), and mp_∞ (green)].

The gating variables *n*, *h*, *e*, and *hp* are slower and have first-order kinetics governed by

$$\frac{\text{d}x}{\text{d}t} = \frac{x_\infty(V) - x}{\tau_x}, \quad x = n,\ h,\ e,\ \text{or } hp, \tag{8}$$

where $x_\infty(V)$ for *n*, *e*, and *hp* is given above by *Eq. 7* and that for h_∞ is given as

$$h_\infty(V) = \frac{\alpha_h(V)}{\alpha_h(V) + \beta_h(V)}, \tag{9}$$

where

$$\alpha_h(V) = 0.128e^{\left(\frac{V+15}{-18}\right)} \tag{10}$$

and

$$\beta_h(V) = \frac{4}{1 + e^{\left(\frac{V+27}{-5}\right)}}. \tag{11}$$

The steady-state activation for the slow variable *n* is shown in Fig. 3*B* (solid magenta), as are the inactivation functions for the slow variables *h* (dotted black), *e* (dotted blue), and *hp* (dotted green). Activation functions are plotted as solid lines, whereas inactivation functions are dotted.

The time constants τ_h and τ_e are given in Table 1, whereas τ_n and τ_{hp} are voltage dependent and given by

$$\tau_x(V) = \frac{\bar{\tau}_x}{\cosh\left(\frac{V - \theta_x}{2\sigma_x}\right)}, \quad x = n \text{ or } hp. \tag{12}$$

LOW-VOLTAGE-ACTIVATED T-TYPE Ca^{2+} CURRENT. The expression for the low-voltage-activated T-type Ca^{2+} current is similar to that given by Terman et al. (2002) except that the single-channel current is described by the Goldman-Hodgkin-Katz formula,

Downloaded from http://jn.physiology.org/ at Florida State University on September 3, 2013

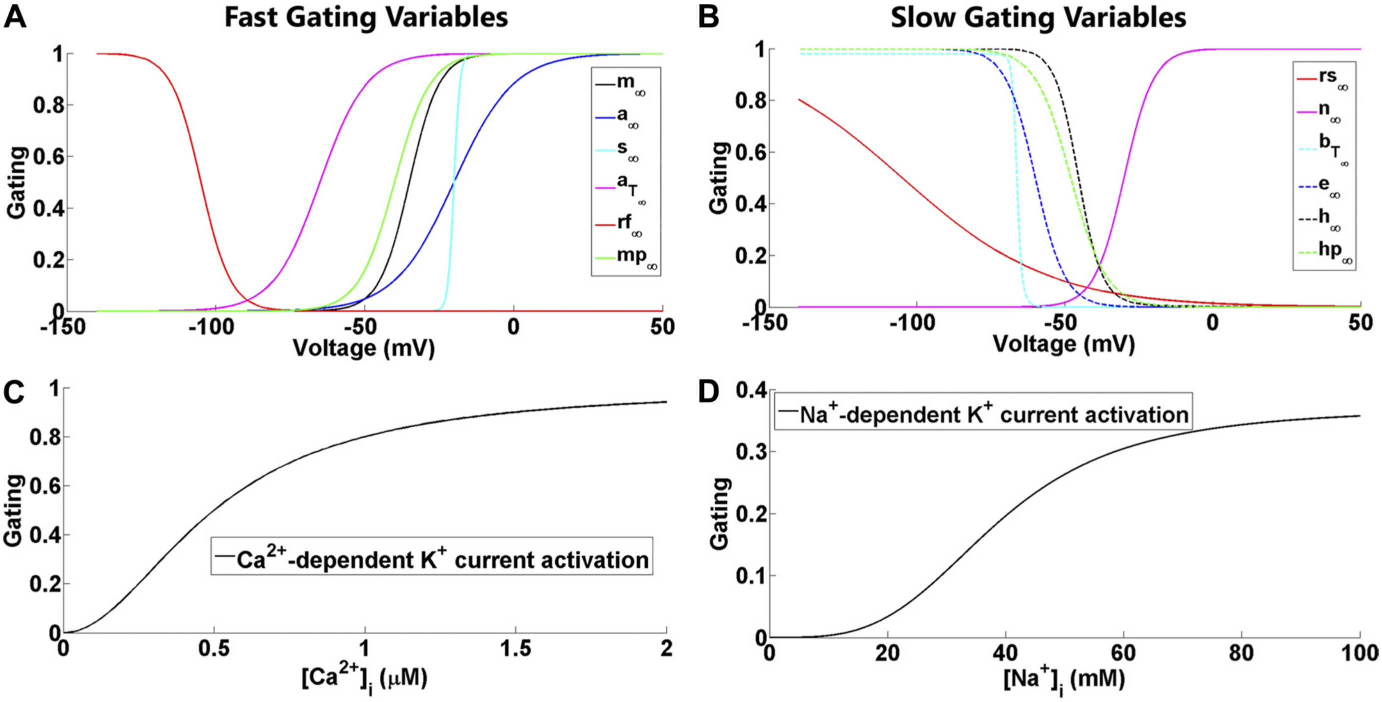

Fig. 3. Steady-state activation functions for the fast gating variables (*A*), the slow gating variables (*B*, solid lines), and the steady-state inactivation functions (*B*, dotted lines). See text for detailed discussion of the functions. *C*: Ca^{2+} dependence of the Ca^{2+}-dependent K^+ current (I_{SK}) gating function. *D*: Na^+ dependence of the Na^+-dependent K^+ current (I_{KNa}).

$$I_{\text{Ca-T}} = g_{\text{Ca-T}}V[a_{\text{T}}]^3_\infty(V)[b_{\text{T}}]^3_\infty(r^{\text{A}}_{\text{T}})\left(\frac{Ca_{\text{ex}}}{1-e^{\frac{2FV}{RT}}}\right). \qquad (13)$$

The activation gating for the rapidly activating channel (a_{T}) is treated as instantaneous (Fig. 3*A*, magenta) and is given by

Table 1. *Parameter values used in all simulations*

Parameter	Value	Parameter	Value
V_{L}	−70 mV	θ_b	0.4 mV
V_{K}	−90 mV	$\theta_{r_{\text{T}}}$	−67 mV
V_{Na}	50 mV	$\theta_{r_{r\text{T}}}$	68 mV
V_{H}	−30 mV	σ_m	−5 mV
g_{L}	2 nS	σ_n	−5 mV
$g_{\text{Ca-L}}$	19 nS	σ_s	−0.05 mV
g_{Nap}	1 nS	σ_{mp}	−6 mV
$\bar{\tau}_n$	10 ms	σ_{hp}	6 mV
$\bar{\tau}_{\text{hp}}$	1,000 ms	σ_a	−10 mV
τ_e	20 ms	σ_e	5 mV
τ_h	1 ms	$\sigma_{r_{\text{f}}}$	5 mV
τ_{r_s}	1,500 ms	$\sigma_{r_{\text{s}}}$	25 mV
τ_{r_0}	200 ms	$\sigma_{a_{\text{T}}}$	−7.8 mV
τ_{r_1}	87.5 ms	σ_b	−0.1 mV
θ_m	−35 mV	$\sigma_{r_{\text{T}}}$	2 mV
θ_n	−30 mV	$\sigma_{r_{r\text{T}}}$	2.2 mV
θ_s	−20 mV	f	0.1
θ_{mp}	−40 mV	ε	0.0015 $\text{pA}^{-1} \cdot \mu\text{M} \cdot \text{ms}^{-1}$
θ_{hp}	−48 mV	k_{Ca}	0.3 ms^{-1}
θ_a	−20 mV	b_{Ca}	0.1 μM
θ_e	−60 mV	k_{s}	0.5 μM
$\theta_{r_{\text{f}}}$	−105 mV	R_{pump}	0.0006 mM/ms
$\theta_{r_{\text{s}}}$	−105 mV	K_p	15 mM
$\theta_{a_{\text{T}}}$	−65 mV	$p_{r_{\text{f}}}$	100

See text for parameter definitions.

$$a_{\text{T}_\infty}(V) = \frac{1}{1+e^{\left(\frac{\text{V}-\theta_{a_{\text{T}}}}{\sigma_{a_{\text{T}}}}\right)}}. \qquad (14)$$

The inactivation variable (b_{T}) is also treated as instantaneous and depends on the slowly operating variable *r*, which reflects the availability of the $I_{\text{Ca-T}}$ current. This is given by

$$b_{\text{T}_\infty}(r_{\text{T}}) = \frac{1}{1+e^{\left(\frac{r_{\text{T}}-\theta_b}{\sigma_b}\right)}} - \frac{1}{1+e^{\left(\frac{-\theta_b}{\sigma_b}\right)}}. \qquad (15)$$

The slowly operating gating variable r_{T} is governed by

$$\frac{\mathrm{d}r_{\text{T}}}{\mathrm{d}t} = \frac{r_{\text{T}_\infty}(V) - r_{\text{T}}}{\tau_{r_{\text{T}}}(V)}, \qquad (16)$$

where

$$r_{\text{T}_\infty}(V) = \frac{1}{1+e^{\left(\frac{V-\theta_{r_{\text{T}}}}{\sigma_{r_{\text{T}}}}\right)}} \qquad (17)$$

and

$$\tau_{r_{\text{T}}}(V) = \tau_{r_0} + \frac{\tau_{r_1}}{1+e^{\left(\frac{V-\theta_{r_{\text{T}}}}{\sigma_{r_{\text{T}}}}\right)}}. \qquad (18)$$

Figure 3*B* shows $b_{\text{T}\infty}$ as a function of voltage when r_{T} is at equilibrium (dotted cyan).

Ca^{2+}-DEPENDENT K^+ CURRENT. The small-conductance Ca^{2+}-dependent K^+ current is modeled as

$$I_{\text{SK}} = g_{\text{SK}}k_\infty([\text{Ca}^{2+}]_{\text{i}})(V - V_{\text{K}}), \qquad (19)$$

where $k_\infty([\text{Ca}^{2+}]_{\text{i}})$ is the steady-state activation function of the SK current that is based on the levels of intracellular calcium (Fig. 3*C*) and is given by

Downloaded from http://jn.physiology.org/ at Florida State University on September 3, 2013

$$k_\infty([\mathrm{Ca}^{2+}]_\mathrm{i}) = \frac{[\mathrm{Ca}^{2+}]_\mathrm{i}^2}{[\mathrm{Ca}^{2+}]_\mathrm{i}^2 + k_\mathrm{s}^2}. \tag{20}$$

The constant k_s is the dissociation constant of the Ca^{2+}-dependent current, and $[\mathrm{Ca}^{2+}]_\mathrm{i}$ is the intracellular concentration of free Ca^{2+} ions and is governed by

$$\frac{\mathrm{d}[\mathrm{Ca}^{2+}]_\mathrm{i}}{\mathrm{d}t} = -f\left\{\varepsilon(I_\text{Ca-L} + I_\text{Ca-T}) + k_\mathrm{Ca}([\mathrm{Ca}^{2+}]_\mathrm{i} - b_\mathrm{Ca})\right\}. \tag{21}$$

The constant f represents the fraction of free-to-total cytosolic Ca^{2+}, whereas the constant ε combines the effects of buffers, cell volume, and the molar charge of calcium. Also, the constant k_Ca is the calcium pump rate constant, and b_Ca represents the basal level of Ca^{2+}.

Na^+-DEPENDENT K^+ CURRENT. The Na^+-dependent K^+ current, modeled as in Wang et al. (2003), is given by

$$I_\mathrm{KNa} = g_\mathrm{KNa} w_\infty([\mathrm{Na}^+]_\mathrm{i})(V - V_\mathrm{K}). \tag{22}$$

The activation function is given by

$$w_\infty([\mathrm{Na}^+]_\mathrm{i}) = \frac{0.37}{1 + \left(\dfrac{38.7}{[\mathrm{Na}^+]_\mathrm{i}}\right)^{3.5}}. \tag{23}$$

and plotted in Fig. 3*D*. $[\mathrm{Na}^+]_\mathrm{i}$ is the intracellular concentration of Na^+ ions and is governed by

$$\frac{\mathrm{d}[\mathrm{Na}^+]_\mathrm{i}}{\mathrm{d}t} = -\alpha_\mathrm{Na}(I_\mathrm{Na} + I_\mathrm{Nap}) - 3R_\mathrm{pump}\left\{\phi_\mathrm{Na}([\mathrm{Na}^+]_\mathrm{i}) - \phi_\mathrm{Na}([\mathrm{Na}^+]_\mathrm{eq})\right\}. \tag{24}$$

The influx of $[\mathrm{Na}^+]_\mathrm{i}$ is controlled by $-\alpha_\mathrm{Na}(I_\mathrm{Na} + I_\mathrm{Nap})$. The Na^+ concentration in HVC neurons has not been measured, so we chose $\alpha_\mathrm{Na} = 0.0001\ \mathrm{mM}\cdot(\mathrm{ms}\cdot\mu\mathrm{A})^{-1}\cdot\mathrm{cm}^2$ so that the increase of $[\mathrm{Na}^+]_\mathrm{i}$ is $\sim$100 μM per action potential, which is similar to what has been reported in hippocampal pyramidal neurons (Jaffe et al. 1992; Rose et al. 1999; Rose and Ransom 1997). The extrusion of $[\mathrm{Na}^+]_\mathrm{i}$ is assumed to be largely due to a Na^+-K^+ ionic pump, which extrudes three Na^+ ions for every two K^+ ions brought into the cell (Fain 1999). The $[\mathrm{Na}^+]_\mathrm{i}$ extrusion by the ion pump was modeled by Li et al. (1996) as $-3R_\mathrm{pump}\{\phi_\mathrm{Na}\ ([\mathrm{Na}^+]_\mathrm{i}) - \text{Ø}_\mathrm{Na}\ ([\mathrm{Na}^+]_\mathrm{eq})\}$, where

$$\phi_\mathrm{Na}(x) = \frac{x^3}{x^3 + K_\mathrm{p}^3}. \tag{25}$$

The sodium concentration at the resting state is assumed to be $[\mathrm{Na}^+]_\mathrm{eq} = 8$ mM. The slow kinetics of the Na^+-K^+ ionic pump are important for the model and play a role in adaptation.

HYPERPOLARIZATION-ACTIVATED INWARD CURRENT. The hyperpolarization-activated inward current's activation is modeled as in Destexhe and Babloyantz (1993) using a fast component (r_f) and a slow component (r_s) as follows:

$$I_\mathrm{h} = g_\mathrm{h}[k_\mathrm{r} r_\mathrm{f} + (1 - k_\mathrm{r}) r_\mathrm{s}](V - V_\mathrm{h}). \tag{26}$$

The fast activation component r_f obeys

$$\frac{\mathrm{d}r_\mathrm{f}}{\mathrm{d}t} = \frac{r_{\mathrm{f}_\infty}(V) - r_\mathrm{f}}{\tau_{r_\mathrm{f}}(V)}, \tag{27}$$

where

$$r_{\mathrm{f}_\infty}(V) = \frac{1}{1 + e^{\left(\frac{V - \theta_{r_\mathrm{f}}}{\sigma_{r_\mathrm{f}}}\right)}} \tag{28}$$

is shown in Fig. 3*A* (red), and its time constant τ_{r_f} is given by

$$\tau_{r_\mathrm{f}}(V) = \frac{p_{r_\mathrm{f}}}{\dfrac{-7.4(V + 70)}{e^{\left(\frac{\mathrm{V}+70}{-0.8}\right)} - 1} + 65e^{\left(\frac{\mathrm{V}+56}{-23}\right)}}. \tag{29}$$

Similarly, the slow activation component r_s obeys

$$\frac{\mathrm{d}r_\mathrm{s}}{\mathrm{d}t} = \frac{r_{\mathrm{s}_\infty}(V) - r_\mathrm{s}}{\tau_{\mathrm{r}_\mathrm{s}}}, \tag{30}$$

where

$$r_{\mathrm{s}_\infty}(V) = \frac{1}{1 + e^{\frac{-(V - \theta_{r_\mathrm{s}})}{\sigma_{r_\mathrm{s}}}}} \tag{31}$$

is shown in Fig. 3*B* (solid red), and τ_{r_s} is given in Table 1.

Manual adjustment of model parameters was performed to qualitatively reproduce membrane potential trajectories. The parameters that were manually adjusted and tuned are listed in Table 2. HVC neurons of the same type behaved similarly in response to depolarizing and hyperpolarizing current pulses, as described earlier. A candidate neuron of each HVC cell type was selected, and the model parameters were fit by eye using iterative manual tuning. For example, the adaptation seen in $\mathrm{HVC_X}$ and $\mathrm{HVC_{RA}}$ neurons was achieved by tuning the g_SK and g_KNa parameters. Similarly, the sag seen in $\mathrm{HVC_X}$ and $\mathrm{HVC_{INT}}$ neurons was achieved by tuning the k_r and g_h parameters. The features that were the target of the fit were the number of spikes, the shape of the spikes, the steepness of the sag, and the strength of the rebound firing.

Fixed parameter values for HVC neurons used in the simulations are given in Table 1. Parameters that vary between the different model neurons are shown in Table 2.

RESULTS

Our goal was to characterize the mix of ionic currents present in $\mathrm{HVC_{RA}}$, $\mathrm{HVC_X}$, and $\mathrm{HVC_{INT}}$ neurons. To facilitate this, we developed biophysical models of the three cell types using current-clamp data and then used these models to predict and interpret the effects of pharmacological blockers. All slice recordings were done using the whole cell patch-clamp technique. These data are based on intracellular recordings from 105 neurons from 34 birds. In the figures, when experimental data were used to calibrate the model, the data are shown first. When the model was used to predict responses to manipulations, the model simulation is shown first.

Table 2. *Parameter values that vary among neuron types*

Parameter	$\mathrm{HVC_X}$	$\mathrm{HVC_{RA}}$	$\mathrm{HVC_{INT}}$
g_Na	450 nS	300 nS	800 nS
g_K	50 nS	400 nS	1700 nS
g_SK	6 nS	27 nS	1 nS
g_KNa	40 nS	500 nS	1 nS
g_h	4 nS	1 nS	4 nS
g_A	5 nS	150 nS	1 nS
$g_\text{Ca-T}$	2.7 nS	0.6 nS	1.1 nS
C_m	100 pF	20 pF	75 pF
k_r	0.3	0.95	0.01

$\mathrm{HVC_X}$, neurons projecting to Area X; $\mathrm{HVC_{RA}}$, neurons projecting to the RA (robust nucleus of arcopallium); $\mathrm{HVC_{INT}}$, HVC interneurons. See text for parameter definitions.

Downloaded from http://jn.physiology.org/ at Florida State University on September 3, 2013

HVC_X Neurons

Response to applied current. The X-projecting neurons (n = 47) have two key identifying features. The first is the spike frequency adaptation observed in response to depolarizing current pulses (Fig. 4*A*). When an HVC_X neuron is stimulated with a relatively weak depolarizing pulse, the neuron fires with high frequency and quickly switches to a lower frequency that gradually decreases over the course of current application (n = 46). The adaptation ratio AR (see *Electrophysiological identification of neurons*) for HVC_X neurons was 3.91 ± 2.1 (n = 13). A second feature of HVC_X neurons is a moderate sag generated in response to hyperpolarizing current pulses (Fig. 4*B*), followed by rebound firing or rebound depolarization on the termination of the pulse (n = 45). The sag and the rebound were larger as for larger hyperpolarization current pulses. The sag ratio SR for this neuronal population (see *Electrophysiological identification of neurons*) was 0.10 ± 0.014 (n = 19). In addition to these two characteristic features that readily identify an HVC_X neuron, a variety of other electrical properties were exhibited as detailed in Table 3. In response to depolarizing current pulses, the spikes emanate from a depolarized plateau (Fig. 4*A*) and exhibit a large-amplitude AHP (14.5 ± 0.4 mV, n = 24) and a slow TTP (13 ± 1.2 ms, n = 26). A subset of the HVC_X neurons (n = 7) exhibited spontaneous firing, which was quickly abolished after dual application of the AMPA/kainate receptor antagonist CNQX (5 μM, n = 4 and 10 μM, n = 3) and the $GABA_A$ receptor antagonist PTX (50 μM, n = 7) (not shown). Spontaneous activity was absent in an additional 14 HVC_X neurons that were recorded in the presence of these receptor antagonists, suggesting that HVC_X neurons are silent in the absence of synaptic drive. These features were useful in distinguishing the X-projecting neurons from the other classes of HVC neurons online, and these classification criteria were confirmed by recording retrogradely labeled HVC_X neurons (Fig. 2*D*).

Next, model HVC_X neuron parameters were calibrated to fit the voltage traces. Figure 4*C* shows the firing pattern of a model HVC_X neuron in response to a 150-pA applied current. The model neuron exhibits spike frequency adaptation that is due to the Ca^{2+}-dependent K^+ current (I_{SK}) and the Na^+-dependent K^+ current (I_{KNa}). The model was also calibrated to fit the sag and the rebound firing seen in HVC_X neurons (Fig. 4*D*). In the model, the sag is primarily due to the I_h current that is activated on hyperpolarization and gradually depolarizes the neuron. The prominence of the sag is controlled by the k_r parameter that governs the weight put on the fast component relative to the slow component of I_h current. For model HVC_X neurons, k_r is set to 0.3, thereby giving 70% of the weight to the slow component of the current that is responsible for the slow depolarization that characterizes the sag. The rebound firing is primarily due to the low-threshold T-type Ca^{2+} current ($I_{Ca\text{-}T}$) in the model, working in cooperation with I_h. The hyperpolarizing current pulse activates I_h and removes the inactivation of $I_{Ca\text{-}T}$. On removal of the hyperpolarizing current, I_h and $I_{Ca\text{-}T}$ together depolarize the cell beyond its resting potential and beyond the spike threshold. The rebound spiking terminates as I_h deactivates and $I_{Ca\text{-}T}$ inactivates. Longer or stronger current application augments deinactivation of $I_{Ca\text{-}T}$, enhancing the rebound.

As a test, we used the calibrated model to predict the average firing frequency over a 1-s duration of applied current for a range of current magnitudes and compared this prediction with the response of actual HVC_X neurons (Fig. 5). Both model and actual neurons had a roughly linear frequency response that ranged from 5 to 40 Hz. Since the frequency response of the model was not a feature used in the calibration, the good fit to

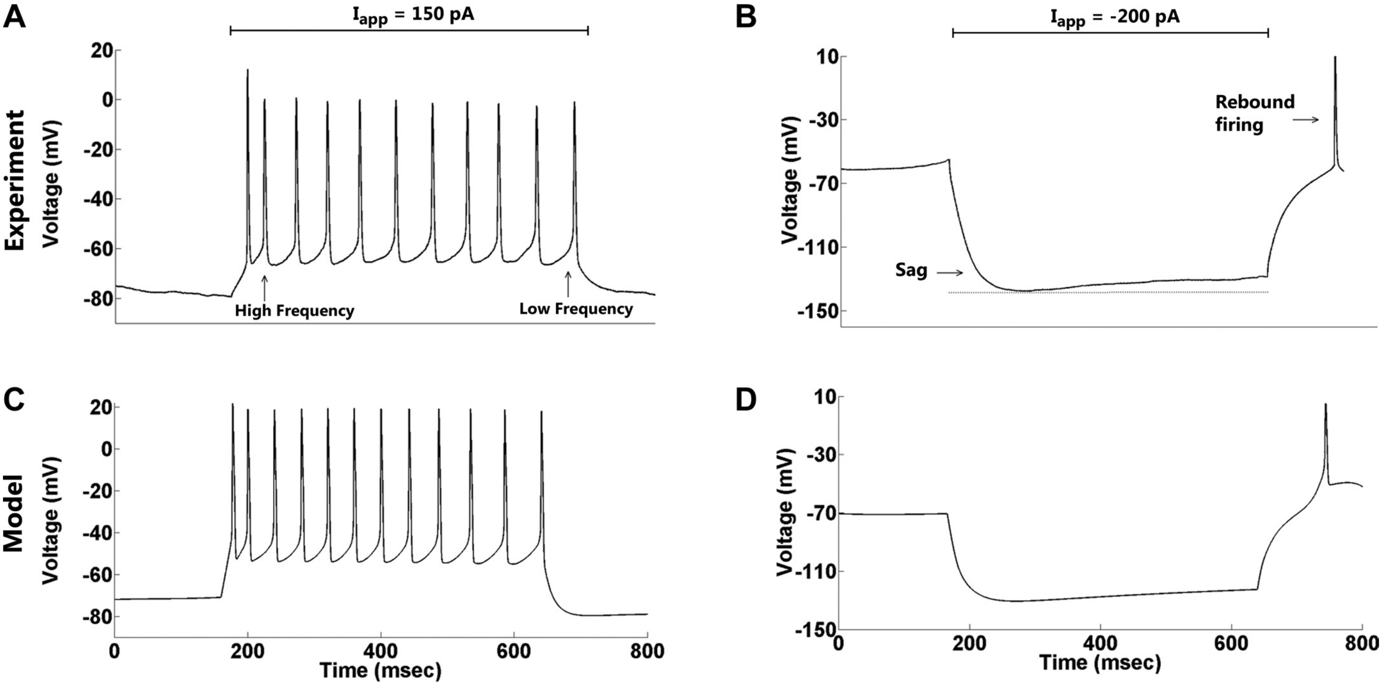

Fig. 4. Firing properties of an X-projecting neuron. *A*: an X-projecting neuron exhibits some spike frequency adaptation in response to a depolarizing current pulse (applied current I_{app} = 150 pA). *B*: a weak sag followed by postinhibitory rebound firing is generated in response to a hyperpolarizing current pulse (−200 pA). *C* and *D*: HVC_X model neuron parameters were calibrated to match the voltage traces. The same magnitude of applied currents used in the slice was used in the model simulations in this and subsequent figures, unless otherwise mentioned.

Downloaded from http://jn.physiology.org/ at Florida State University on September 3, 2013

Table 3. *Experimental characterization of the three types of HVC neurons*

Electrophysiological Property	Blocked by Drug(s)
HVC$_{X}$ neurons	
Spike frequency adaptation (46/47)	
Spike from depolarized plateau (42/47)	
Large AHP (24/47)	Apamin (4/4)
Slow TTP (26/47)	
AR of 3.91 ± 2.1 (n = 13)	
Moderate sag (45/47)	ZD 7288 (8/8)
SR of 0.10 ± 0.014 (n = 19)	
Rebound firing (35/47)	Mibefradil (6/7)
Rebound depolarization (9/47)	Mibefradil and ZD 7288 (3/3)
Spontaneous activity (7/47)	CNQX and PTX (7/7)
HVC$_{RA}$ neurons	
Low excitability (33/33)	Apamin (6/6), quinidine (3/3)
Delayed spike (14/33)	4-AP (5/8)
Spikes from depolarized plateau (32/33)	
Fast large AHP (17/33)	4-AP (4/8)
Fast TTP (19/33)	
Absence of sag (33/33)	
SR of 0.009 ± 0.003 (n = 11)	
Fast inward rectification (23/23)	
Absence of rebound firing (30/33)	
Hyperpolarized RMP (33/33)	Apamin (6/6), quinidine (3/3), 4-AP (8/8)
HVC$_{INT}$ neurons	
High firing frequency (25/25)	
Sharp downstrokes of AP (25/25)	
Spike amplitude of 78 ± 5 mV (18/25)	
Spike amplitude of 55 ± 8 mV (7/25)	
Large AHP (16/25)	
Short TTP (17/25)	
Prominent sag (25/25)	ZD 7288 (5/5)
SR of 0.24 ± 0.065 (n = 9)	
Rebound firing (25/25)	Mibefradil (4/4) and ZD 7288
Spontaneous activity (18/25)	

Values for (x/y) indicate that x neurons of y neurons tested exhibit the corresponding property; n is the no. of neurons used to calculate the corresponding ratio. AHP, after hyperpolarization; TTP, time to peak; AR, adaptation ratio; SR, sag ratio; RMP, resting membrane potential; AP, action potential; CNQX, 6-cyano-7-nitroquinoxaline-2,3-dione; PTX, picrotoxin; 4-AP, 4-aminopyridine.

experimental data provides support for the model and the manner in which it was calibrated.

H current and inward rectification in HVC$_{X}$ neurons. The sag and postinhibitory rebound produced by HVC$_{X}$ neurons are examined further in Fig. 6. Figure 6*A* shows the current-voltage relationship of the model HVC$_{X}$ neuron, using the same parameters as in Fig. 4. The curve with circles represents the voltage at the end of the hyperpolarizing current pulses, whereas the curve with triangles is the voltage at the nadir. As the magnitude of the current pulse increases, the difference between the voltage responses at the end of the current pulse and at its nadir increases, indicating an increase in the sag. In the slice, HVC$_{X}$ neurons showed a similar behavior (n = 35). A representative example is shown in Fig. 6*B*.

The sag generated in the model HVC$_{X}$ neuron is due to the hyperpolarization-activated inward current, I_{h} (Fig. 6*C*), which also contributes to the rebound (black trace). The *inset* of Fig. 6*C* shows the total I_{h} conductance, g_{h}. It is near 0 at rest but increases on hyperpolarization. The fast component causes a rapid initial increase in g_{h}, followed by a slower rise due to the slow component. This slow rise is reflected in the voltage as a sag. When the current pulse is terminated, the rapid component of g_{h} quickly goes to 0, whereas the slow component remains. It is this residual slow component that contributes to the rebound firing.

Blockade of I_{h} is simulated in the model by setting g_{h} to 0. This results in a small decline in the resting membrane potential and a much larger hyperpolarization during the current pulse (Fig. 6*C*, red trace). This reflects the absence of the fast component of I_{h}. The sag is gone and there is no rebound, reflecting the absence of the slow component of I_{h}. There is, however, a small voltage rebound depolarization due to the $I_{\text{Ca-T}}$ current, as discussed below.

Model predictions were tested and verified in the slice by pharmacologically blocking I_{h} using ZD 7288 (50 μM; Fig. 6*D*). ZD 7288 application eliminated the sag and the weak rebound firing but retained a small rebound depolarization (Fig. 6*D*, red trace, 20 min after drug application) in the same X-projecting cell used in Fig. 4*B*. Moreover, the resting membrane potential was hyperpolarized by ~5 mV. Similar behavior was observed in all of the seven additional HVC$_{X}$ neurons examined, two of which were given a lower concentration of ZD 7288 (30 μM). Therefore, the sag seen in HVC$_{X}$ neurons is due to the hyperpolarization-activated inward current, which also contributes to rebound firing.

Actions of I_{h} and $I_{Ca\text{-}T}$ in HVC$_{X}$ neurons. The interplay between the I_{h} and $I_{\text{Ca-T}}$ currents and their role in shaping the firing pattern of HVC$_{X}$ neurons was further examined. Figure 7*A* shows a model HVC$_{X}$ neuron exhibiting a sag and rebound firing (black trace, g_{K} = 1,700 nS, g_{SK} = 1 nS, I_{app} = −120 pA). Setting $g_{\text{Ca-T}}$ to 0 eliminates the rebound firing and any rebound depolarization (not shown). The rebound firing can be eliminated and a voltage depolarization retained by partial blockade of $I_{\text{Ca-T}}$ ($g_{\text{Ca-T}}$ = 0.1 nS, 3.7% of original conductance), which leaves the sag unaltered (red trace). The sag and rebound depolarization are eliminated by additional blockade of I_{h} (g_{h} = 0 nS, green trace). The *inset* of Fig. 7*A* shows the total $I_{\text{Ca-T}}$ current conductance ($g_{\text{Ca-T}}$) in the model HVC$_{X}$ neuron under the three conditions. The conductance is near 0 during the hyperpolarization, since the channel is deactivated. However, it also loses any inactivation, so when the applied hyperpolarizing current is removed, the $I_{\text{Ca-T}}$ current quickly activates and depolarizes the cell to spike threshold (black trace). When the current is mostly blocked (red trace), its residual total conductance has sufficient strength to activate and depolarize the model cell; however, it is still too small to bring the cell to spike threshold. When I_{h} is blocked, the voltage does not go high enough after the pulse termination to activate the $I_{\text{Ca-T}}$ current, so $g_{\text{Ca-T}}$ remains low.

Model predictions were matched in the slice by blocking $I_{\text{Ca-T}}$ (Fig. 7*B*, red trace) using mibefradil (6 μM, 40 min after drug application, I_{app} = −120 pA) (Lacinova 2004, 2005). Mibefradil kept the sag intact, eliminated the rebound firing, and left a rebound depolarization. A subsequent application of ZD 7288 (50 μM, 30 min after ZD 7288 application) to block I_{h} eliminated the sag and the rebound depolarization (green trace). Similar results were observed in two other HVC$_{X}$ neurons that were tested. Mibefradil eliminated rebound spiking in three additional neurons, reaffirming that rebound firing

Downloaded from http://jn.physiology.org/ at Florida State University on September 3, 2013

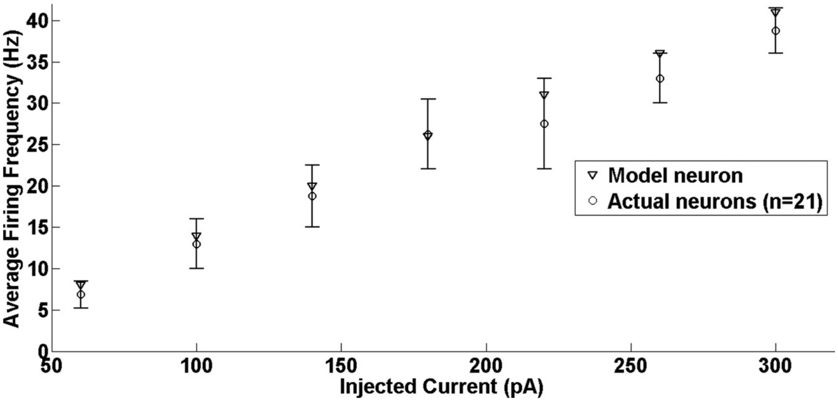

Fig. 5. The firing frequency of a model HVC_X neuron under various current injections (triangles) closely matches the data from X-projecting neurons in the slice (circles, n = 21). Data are means ± SE. For both model and actual HVC_X neurons, the duration of applied current was 1 s.

in these neurons requires the low-threshold T-type Ca^{2+} current.

I_{SK} and I_{KNa} in HVC_X neurons. The spike frequency adaptation seen in HVC_X neurons was further examined. Figure 8*A* shows a model HVC_X neuron exhibiting adaptation, using the same parameters as in Fig. 4 but with g_{Na} = 800 nS and g_{SK} = 5 nS. Blocking the Ca^{2+}-dependent K^+ current by setting its conductance (g_{SK}) to 0 increases the model neuron's excitability slightly, but the adaptation is retained due the presence of the Na^+-dependent K^+ current (Fig. 8*C*). Moreover, the resting membrane potential increased by a few millivolts (~3 mV), and the shape of the interspike voltage time course has changed.

Model predictions were tested in the slice by blocking I_{SK} using apamin (150 nM). Figure 8*B* shows a HVC_X neuron exhibiting spike frequency adaptation. Apamin application had little effect on adaptation and changed the shape of the interspike voltage time course, as in the model (Fig. 8*D*). Moreover, the resting membrane potential was depolarized by ~5 mV. Unlike the model response however, apamin application reduced the AHP following each action potential significantly. Similar results were observed in three additional HVC_X neurons that were tested.

These results suggest that the spike frequency adaptation in HVC_X neurons is not mediated by SK current, but the AHP following each action potential is. This agrees well with findings of Kubota and Saito (1991) and Schmidt and Perkel (1998). The former identified a Na^+-dependent K^+ conductance in HVC neurons, but because of the nonselectivity of pharmacological blockers of I_{KNa}, we did not pursue this further.

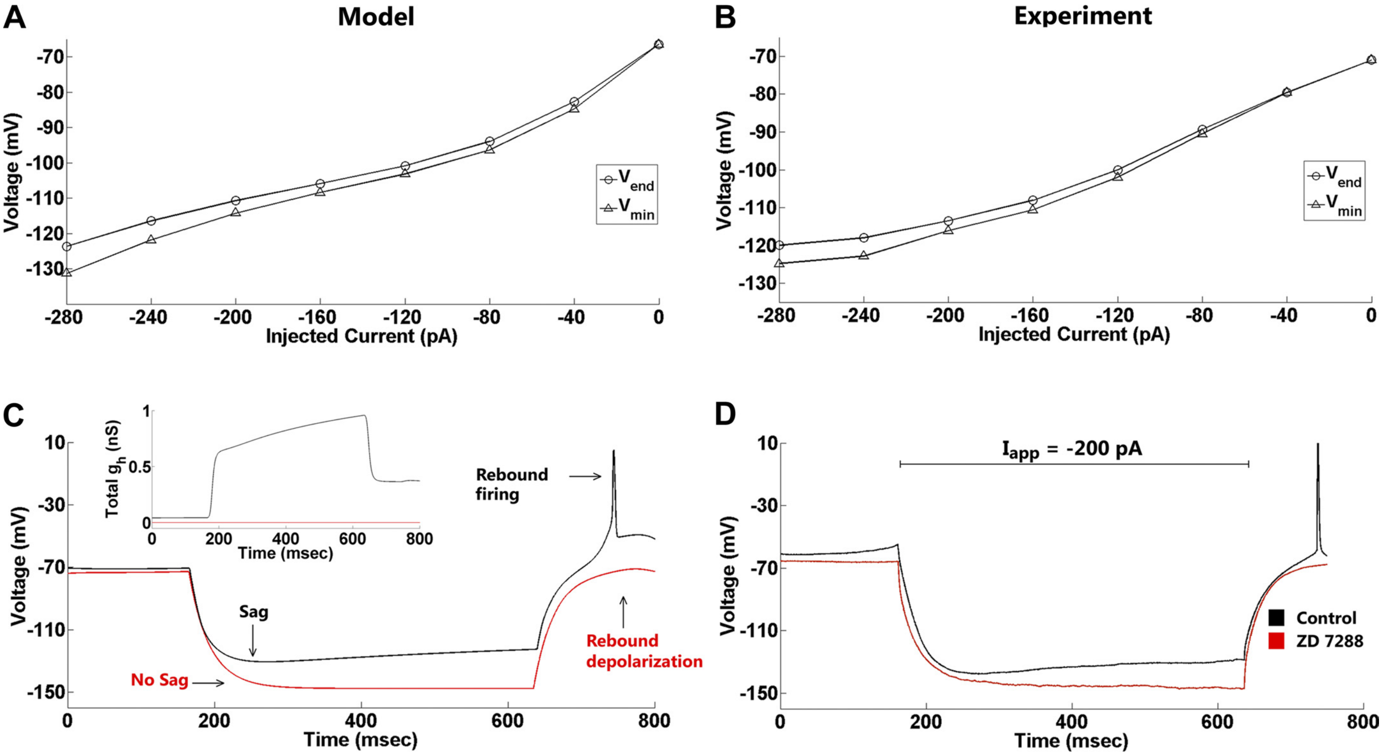

Fig. 6. Inward rectification and hyperpolarization-activated inward current (I_h) in HVC_X neurons. *A*: current-voltage relationship of a model HVC_X neuron using the same parameters as in Fig. 4. Circles with solid curve represent voltage responses measured at the end of the current pulses, whereas triangles with solid curve represent voltage at the nadir. *B*: current-voltage relationship for an HVC_X neuron. *C*: the sag generated in the model HVC_X neuron is due to I_h (with g_h = 4 nS), which is contributing partially to the rebound spike (black trace). Blocking I_h by setting its conductance (g_h) to 0 eliminated the sag but kept a small rebound depolarization due to low-threshold T-type Ca^{2+} current ($I_{Ca\text{-}T}$; red trace). *Inset* shows the total I_h conductance (g_h). *D*: blocking I_h using ZD 7288 (50 μM) eliminated the sag and the rebound firing (red trace, 20 min after ZD 7288 application) in the same X-projecting cell used in Fig. 4*B*, matching model predictions.

Downloaded from http://jn.physiology.org/ at Florida State University on September 3, 2013

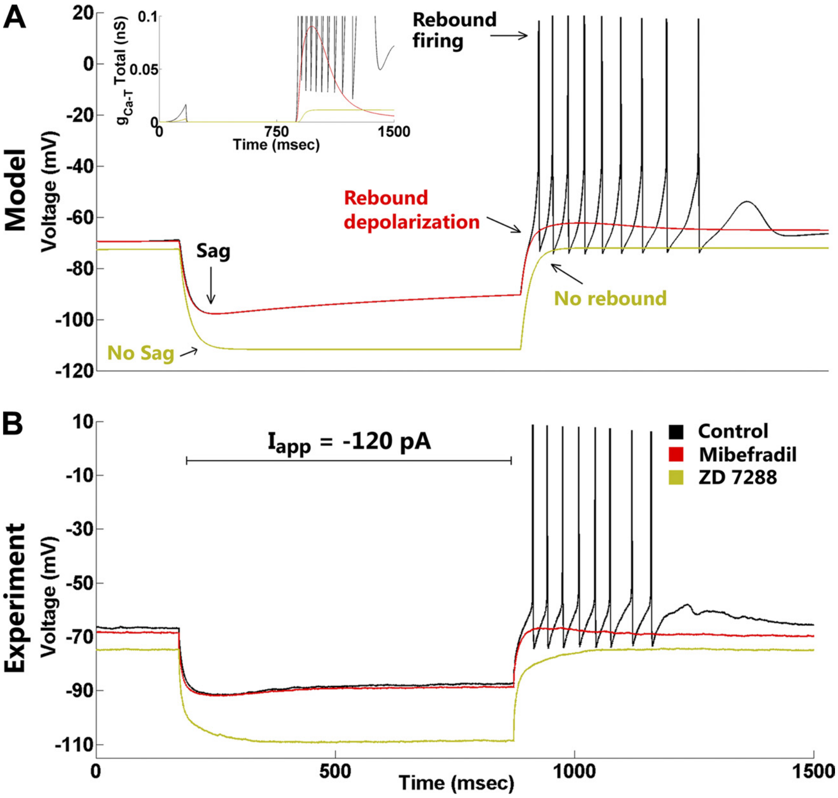

Fig. 7. I_h and $I_{Ca\text{-}T}$ mechanisms in HVC_X neurons. *A*: black trace shows a model HVC_X neuron exhibiting a sag and rebound firing (g_K = 1,700 nS, g_{SK} = 1 nS, I_{app} = −120 pA). The rebound firing is eliminated by partial blockade of $I_{Ca\text{-}T}$ ($g_{Ca\text{-}T}$ = 0.1 nS, 3.7% of original conductance), leaving a small rebound depolarization and keeping the sag intact (red trace). The sag and rebound depolarization are eliminated by additional blockade of I_h (g_h = 0 nS; green trace). *Inset* shows the total $I_{Ca\text{-}T}$ current conductance ($g_{Ca\text{-}T}$) in the model HVC_X neuron under the 3 conditions. *B*: in an HVC_X neuron, model predictions were matched by blocking $I_{Ca\text{-}T}$ (red trace) using mibefradil (6 μM, 40 min after drug application, I_{app} = −120 pA). A subsequent application of ZD 7288 (50 μM, 30 min after ZD application) to block I_h eliminated the sag and the rebound depolarization (green trace).

HVC_{RA} Neurons

Response to applied current. The RA-projecting neurons (n = 33) have three key identifying features. The first is their relative lack of excitability in response to depolarizing current pulses (Fig. 9*A*). The neuron fires with one (n = 17) or few spikes (n = 12) in response to a relatively large depolarizing pulse. The second is the absence of sag in response to hyperpolarizing current pulses (n = 33; Fig. 9*B*), along with an absence of rebound firing on the termination of the hyperpolarizing pulses (n = 30). The SR in HVC_{RA} neurons was 0.009 ± 0.003 (n = 11). In a small subset of these neurons, however, a small rebound depolarization was seen (n = 3). The third identifying feature is the extremely hyperpolarized resting membrane potential of −85 ± 6 mV (n = 33). In addition to these features, the firing pattern of RA-projecting neurons exhibits other important characteristics (Table 3). There is often a delay to spiking in response to depolarization (n = 14). In a subset of these neurons, tonic firing was observed (n = 4). Moreover, the spikes emanate from a depolarized plateau but have sharp downstrokes, where each spike is followed by a fast AHP that exhibits a large amplitude (16 ± 0.8 mV, n = 17) and a short TTP (3 ± 0.4 ms, n = 19). Although no sag is present in response to hyperpolarizing current pulses, the fact that the spacing between voltage traces becomes smaller with greater hyperpolarizing currents indicates that there is fast inward rectification (n = 23). That is, a depolarizing current is being activated at the lower voltages. These features were very useful in distinguishing the RA-projecting neurons from the other classes of HVC neurons online, and these classification criteria were confirmed by recording retrogradely labeled HVC_{RA} neurons (Fig. 2*E*).

Model HVC_{RA} neuron parameters were calibrated to fit the voltage traces in response to a depolarizing and a hyperpolarizing current pulse. Figure 9*C* shows the firing pattern of a model HVC_{RA} neuron in response to a 150-pA applied current. The model neuron exhibits delay to spiking that is due to the A-type K^+ current (I_A), which contributes to the lack of excitability with the cooperation of I_{SK} and I_{KNa}. The *inset* of Fig. 9*C* shows the total I_A current conductance, g_A. It is near 0 at rest but increases rapidly on depolarization due to fast activation. This rapid increase halts after a few milliseconds and switches to a slow decrease that is due to slow inactivation. The slow decrease is reflected in the voltage trace as a slow depolarization in the membrane potential, and this allows the model neuron to escape the inhibition produced by I_A and fire a delayed spike.

The model was also calibrated to fit the voltage response to hyperpolarizing currents (Fig. 9*D*). In the model, the absence of the sag is primarily due to the large value of k_r, which is set to 0.95, thereby giving almost all the weight to the fast component of the I_h current and very little to the slow component. The absence of the rebound is due to the small values of the $I_{Ca\text{-}T}$ current conductance ($g_{Ca\text{-}T}$ = 0.55 nS) and I_h current conductance (g_h = 1 nS), which prevent the model cell from depolarizing beyond its resting potential and spike threshold. The small I_h that is present, however, is sufficient to produce inward rectification of the membrane on hyperpolarization; as the membrane is hyperpolarized to lower voltages, I_h activation increases, reducing the spacing between the voltage curves. If g_h is set to 0, inward rectification disappears and the spacing between the voltage traces becomes equal in response to equal steps of hyperpolarizing current pulses (not shown).

Downloaded from http://jn.physiology.org/ at Florida State University on September 3, 2013

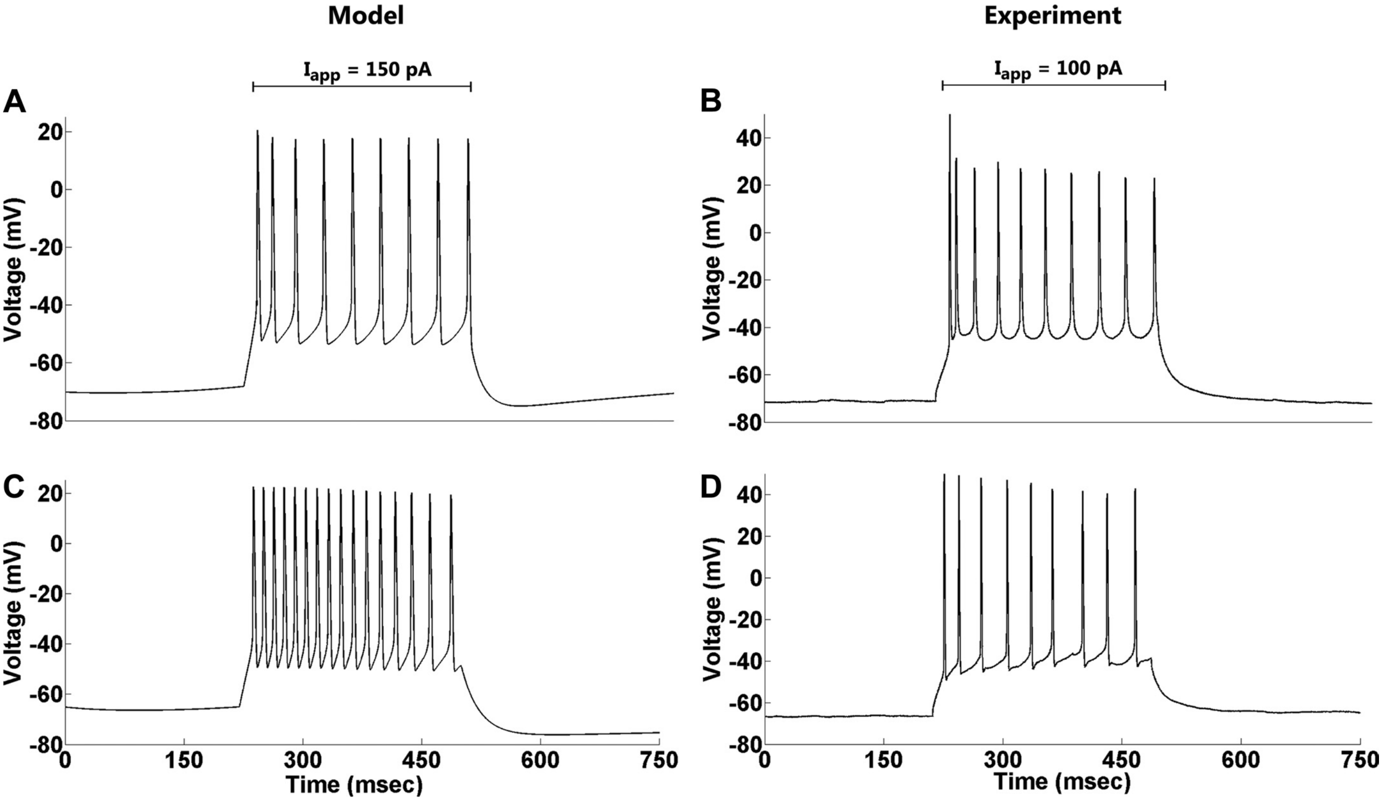

Fig. 8. Effect of I_{SK} in HVC$_X$ neurons. *A*: a model HVC$_X$ neuron exhibits spike frequency adaptation (I_{app} = 150 pA). *B*: an X-projecting neuron exhibits adaptation for a current pulse of 100 pA. *C*: blocking I_{SK} by setting its conductance (g_{SK}) to 0 increases the model neuron's excitability slightly, but the adaptation is preserved. Also, the resting membrane potential is increased by a few millivolts (~3 mV), and the interspike voltage time course has changed its shape. *D*: blocking I_{SK} using apamin (150 nM) had little effect on adaptation, changed the shape of the interspike voltage time course, and reduced the afterhyperpolarization (AHP) following each action potential. It also depolarized the resting membrane potential by ~5 mV.

We used the model neuron to predict the average firing frequency over a 1-s duration of applied current for a range of current magnitudes and compared this prediction with the response of actual HVC$_{RA}$ neurons (Fig. 10). Both model and actual HVC$_{RA}$ neurons had a roughly linear frequency response that ranged from 3 to 25 Hz. For $I_{app} \leq 50$ pA, both model and actual HVC$_{RA}$ neurons did not spike during the depolarization, so no average firing frequency was computed. For I_{app} = 100 pA, the model neuron showed no activity, but the actual neurons fired with very low frequency. Overall, the predicted model neuron response agreed well with the frequency responses of the actual HVC$_{RA}$ neurons (n = 6).

I_A current in HVC$_{RA}$ neurons. The delay to spiking in HVC$_{RA}$ neurons was further examined. Figure 11*A* shows a model HVC$_{RA}$ neuron with delay to spiking (g_{KNa} = 1,000 nS, I_{app} = 200 pA). Setting g_A to 0 eliminates the delay and increases excitability (Fig. 11*C*). Moreover, the resting membrane potential is slightly depolarized when I_A is eliminated.

Figure 11, *B* and *D*, shows an HVC$_{RA}$ neuron before (*B*) and after (*D*) application of the I_A blocker 4-AP (0.3 mM, I_{app} = 200 pA). Drug application eliminated the delay to spiking, increased the neuron's firing frequency, and left a strong adaptation. Moreover, the resting membrane potential was depolarized by ~3 mV. Unlike the model response, however, 4-AP reduced the AHP following each spike. Similar results were observed in four additional HVC$_{RA}$ neurons that were tested.

Larger dosages of 4-AP as well as long durations of application switched the neurons' firing pattern from tonic spiking to episodes of large plateau oscillations (n = 3). Similar oscillations were observed following application of quinidine (250 μM) in an attempt to block I_{KNa} pharmacologically. This also caused a dramatic increase in the resting membrane potential (~12 ± 3 mV increase; data not shown). Quinidine is known to be a nonselective blocker of K$^+$ currents, as is 4-AP at high dosages. It is therefore hard to know what mixture of blocked currents produces this behavior. Bursting patterns were produced in our model HVC$_{RA}$ neuron by setting g_A = g_{KNa} = 0 and reducing the magnitude of g_K to 15 nS. However, this bursting pattern did not fully resemble the plateau oscillations produced by the actual neuron. Because of the ambiguity in current blockage, we did not pursue this further.

I_{SK} current in HVC$_{RA}$ neurons. We next investigated what role the Ca^{2+}-dependent K$^+$ current plays in the lack of excitability of HVC$_{RA}$ neurons. Figure 12*A* shows a model HVC$_{RA}$ neuron using the same parameters as in Fig. 9*C*, but with g_{KNa} = 100 nS, g_A = 0 nS, g_{SK} = 35 nS, and $g_{Ca\text{-}T}$ = 6 nS. Blocking I_{SK} (g_{SK} = 0) caused a dramatic increase in excitability, decreased the spike amplitude slightly, and increased the resting membrane potential by ~8 mV (Fig. 12*C*).

Figure 12*B* shows an actual HVC$_{RA}$ neuron's response to 150 pA. This neuron does not exhibit a delay to spiking (n = 12 HVC$_{RA}$ neurons had no delay). Application of apamin (150 nM) greatly increased the neuron's excitability, decreased the spike amplitude, and depolarized the resting membrane poten-

Downloaded from http://jn.physiology.org/ at Florida State University on September 3, 2013

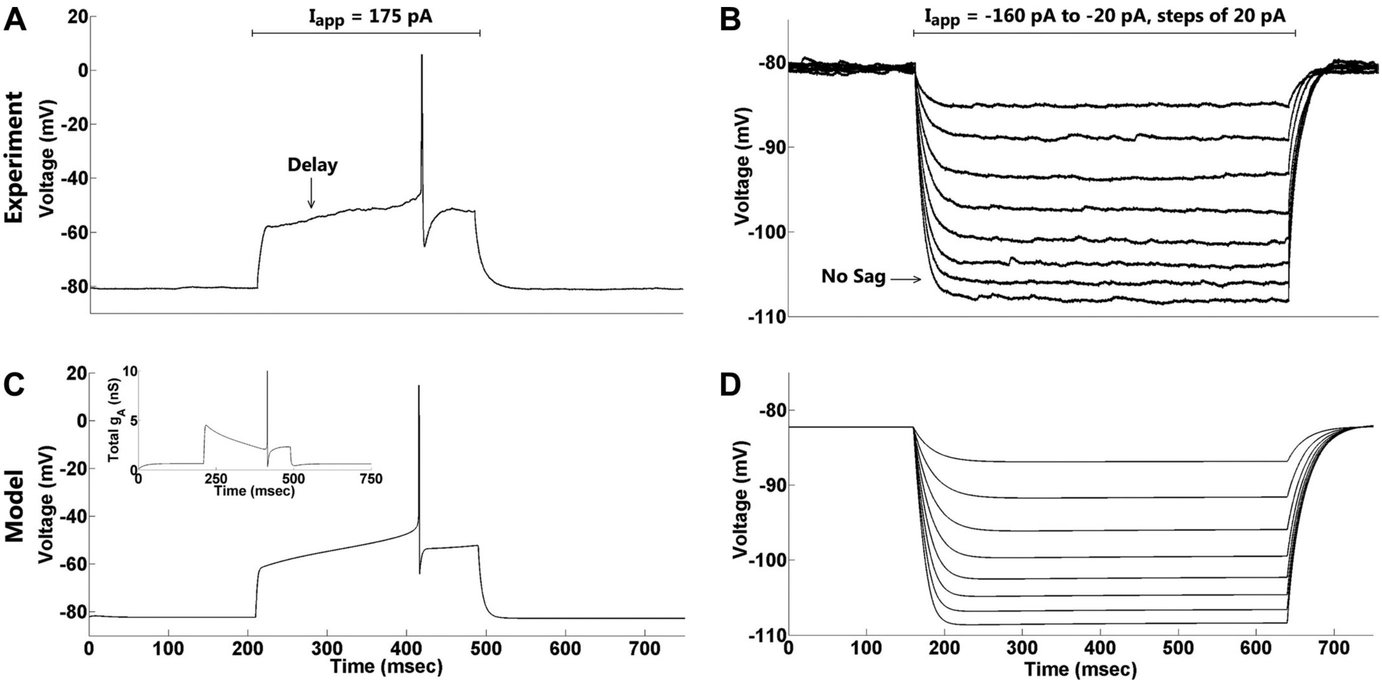

Fig. 9. Firing properties of an RA-projecting neuron. *A*: an RA-projecting neuron fires a single action potential, often with a long delay, in response to a relatively large depolarizing pulse (175 pA). *B*: no sag is present in response to hyperpolarizing current pulses (−160 to −20 pA, in steps of 20 pA). *C*: HVC_{RA} model neuron parameters were calibrated to match the experimental recording (I_{app} = 150 pA). The long delay to spiking is due to the A-type K^+ current (I_A). *Inset* shows the total I_A conductance (g_A) during the current pulse. *D*: for the same parameter values used in *C*, the HVC_{RA} model neuron has no sag but exhibits inward rectification in the spacing between voltage traces, as in *B*.

tial by ~5 mV (Fig. 12*D*). However, unlike the model response, no adaptation was seen (AR = 1.04). Similar results were observed in three additional HVC_{RA} neurons (one where adaptation was present). In two other HVC_{RA} neurons, apamin application had similar effects, but there was a very high plateau potential and the amplitude of the spikes was much smaller.

These results show that the SK current plays a key role in damping the excitability of HVC_{RA} neurons. It also contributes to maintaining the extremely negative resting membrane potential of these neurons.

HVC_{INT} Neurons

Response to applied current. HVC interneurons were less frequently encountered (*n* = 25) and have two identifying features. The first is the high firing frequency observed in response to depolarizing current pulses (Fig. 13*A*). When an HVC_{INT} neuron is stimulated with a very small depolarizing pulse, the neuron fires with high frequency (*n* = 25). A second identifying feature is a prominent sag generated in response to hyperpolarizing current pulses (Fig. 13*B*), followed by rebound firing on the termination of the pulse (*n* = 25). The SR for this neuronal population was 0.24 ± 0.065 (*n* = 9). Other features of HVC_{INT} neuron firing patterns are described in Table 3. In response to depolarizing current pulses, the spikes were followed by a large-amplitude AHP (23 ± 0.7 mV, *n* = 16) with a short TTP (4 ± 0.5 ms, *n* = 17). Most of the interneurons seen had spikes that overshot 0 mV (*n* = 18, spike amplitude = 78 ± 5 mV), but in a subset of neurons the spikes remained below 0 mV (*n* = 7, spike amplitude = 55 ± 8 mV). Moreover, 18 interneurons fired spontaneously with a variety of patterns. Figure 14 shows a sample of four different HVC_{INT} neurons firing spontaneously over long periods of time (~2.5 min). Unlike HVC_X neurons, this spontaneous activity was reduced, but not abolished,

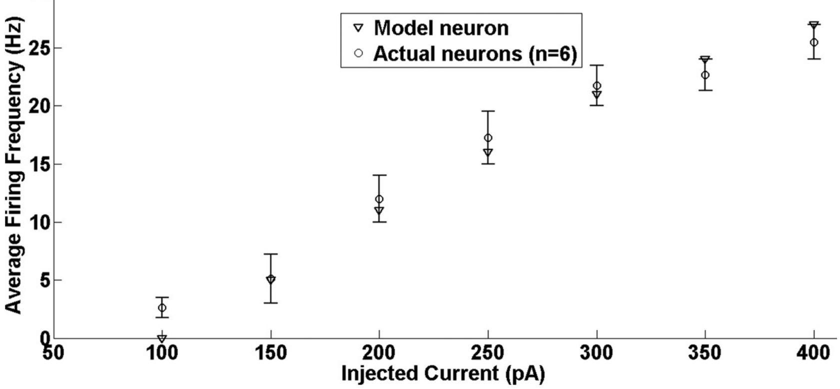

Fig. 10. The firing frequency of a model HVC_{RA} neuron under various current injections (triangles) closely matches the data from RA-projecting neurons in the slice (circles, *n* = 6). Values are means ± SE. For both model and actual HVC_{RA} neurons, the duration of applied current was 1 s.

Downloaded from http://jn.physiology.org/ at Florida State University on September 3, 2013

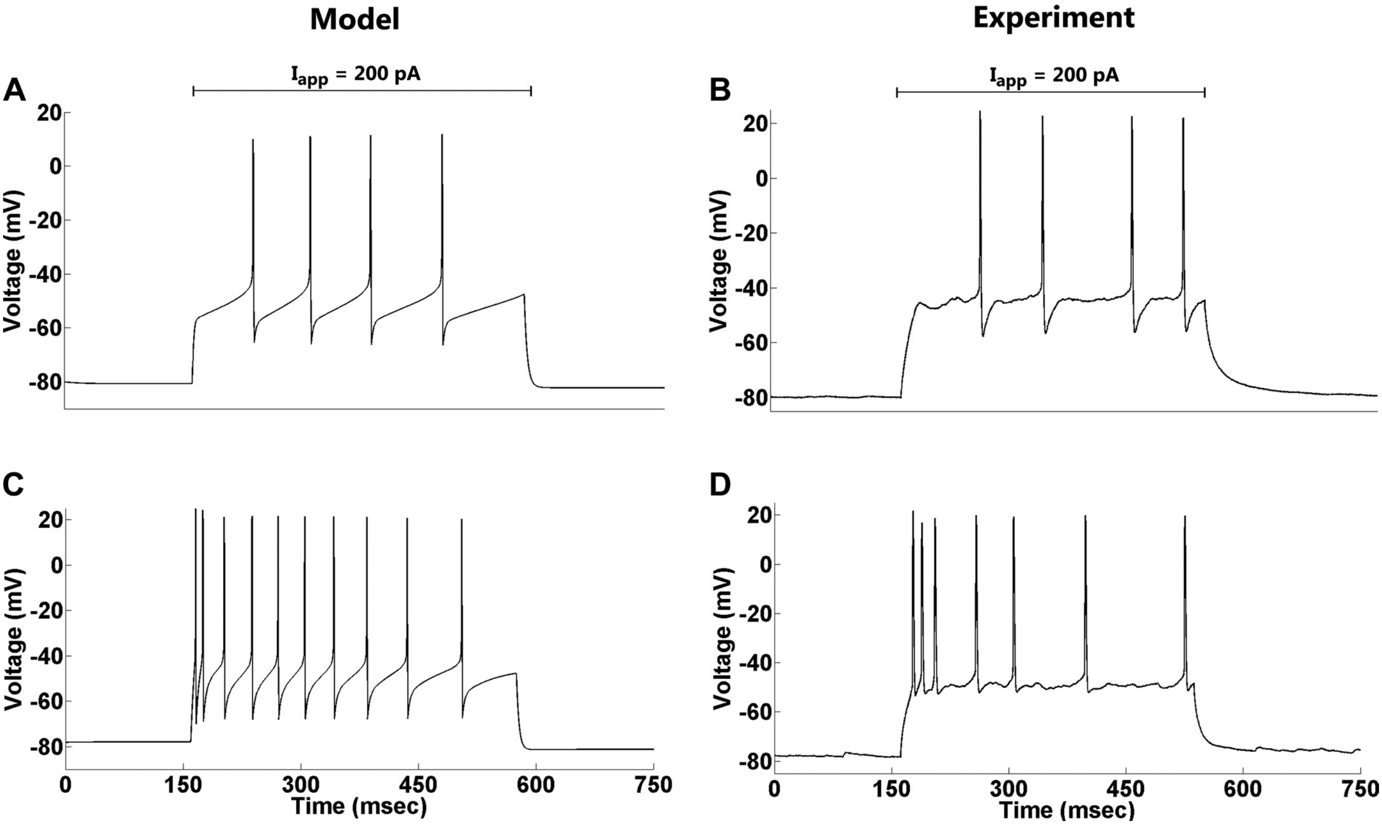

Fig. 11. Effect of I_A in HVC$_{RA}$ neurons. *A*: in a model HVC$_{RA}$ neuron there is a delay to spiking following application of a depolarizing current (I_{app} = 200 pA). *B*: an RA-projecting neuron exhibits a delay to spiking following application of a depolarizing current (200 pA). *C*: blocking I_A eliminates the delay to spiking. The adaptation present at the beginning of the voltage trace after blockade is due to the Na$^+$-dependent and Ca^{2+}-dependent K$^+$ currents. *D*: model predictions were verified experimentally by the application of 4-aminopyridine (4-AP; 0.3 mM), which eliminated the delay to spiking. The resting membrane potential increased after drug application in both the model and the actual cell.

after CNQX (5 μM) and PTX (50 μM) application to block synaptic input (n = 4; not shown).

Model HVC$_{INT}$ neuron parameters were calibrated to fit the voltage traces in response to depolarizing and hyperpolarizing current pulses (but not the spike amplitudes, which fall into 2 classes). Figure 13*C* shows the firing pattern of a model HVC$_{INT}$ neuron in response to a 75-pA applied current. The model neuron exhibits high firing frequency and no adaptation, both features that are due to the very small magnitudes of the I_{SK} and I_{KNa} conductances, thereby increasing the excitability of the model cell. Moreover, the model HVC$_{INT}$ neuron undershoots the resting membrane potential because of the relatively large magnitude of the delayed-rectifier K$^+$ current conductance. The model was also calibrated to fit the sag and the rebound firing seen in HVC$_{INT}$ neurons (Fig. 13*D*). As with the HVC$_X$ model neuron, the sag in the HVC$_{INT}$ model neuron is due to I_h, which is activated on hyperpolarization and gradually depolarizes the neuron. The prominence of the sag is primarily due to the extremely small value of k_r (0.01), thereby giving almost all the weight to the slow component of the I_h current. Also, similar to the HVC$_X$ model neuron, the rebound firing is due to $I_{Ca\text{-}T}$ and I_h. Model HVC$_{INT}$ neurons, however, do not generate the spontaneous firing seen in HVC$_{INT}$ neurons (Fig. 14).

The model HVC$_{INT}$ neuron was used to predict the average firing frequency over a 1-s duration of applied current for a range of current magnitudes and compared with the response of actual HVC$_{INT}$ neurons (Fig. 15). The frequency was much higher than in other HVC neurons, ranging from 10 to 70 Hz. The predicted model neuron response agreed well with the frequency responses of the actual HVC$_{INT}$ neurons (n = 15).

H current and inward rectification in HVC$_{INT}$ neurons. The sag and rebound of HVC$_{INT}$ neurons are examined further in Fig. 16. The current-voltage relationship of the model HVC$_{INT}$ neuron is shown in Fig. 16*A*. The solid curve with circles represents the voltage at the end of the current pulses, whereas the dashed curve with triangles is the voltage at the nadir. The difference between the voltage responses at the end of the current pulse and at its nadir, i.e., the sag, increases as the magnitude of the hyperpolarizing current pulse increases. This difference is much larger than that seen in HVC$_X$ neurons (compare with Fig. 6*A*). In the slice, HVC$_{INT}$ neurons showed a similar behavior (n = 18). A representative example is shown in Fig. 16*B*.

Similar to that in HVC$_X$ neurons, the sag generated in the model HVC$_{INT}$ neuron is due to the hyperpolarization-activated inward current (Fig. 16*C*). The *inset* of Fig. 16*C* shows the total I_h conductance, g_h. Because the HVC$_{INT}$ resting membrane potential is relatively high (approximately −65 mV), some I_h conductance is activated at rest. In contrast, the resting level of g_h was almost 0 in the model HVC$_X$ neuron (see Fig. 6*C*, *inset*), since the resting membrane potential was lower. When the hyperpolarizing pulse is applied, g_h slowly rises, resulting in a voltage sag. The increase is slow, since g_h is dominated by the slow component in this model neuron. When the current pulse is terminated, the slow component of

Downloaded from http://jn.physiology.org/ at Florida State University on September 3, 2013

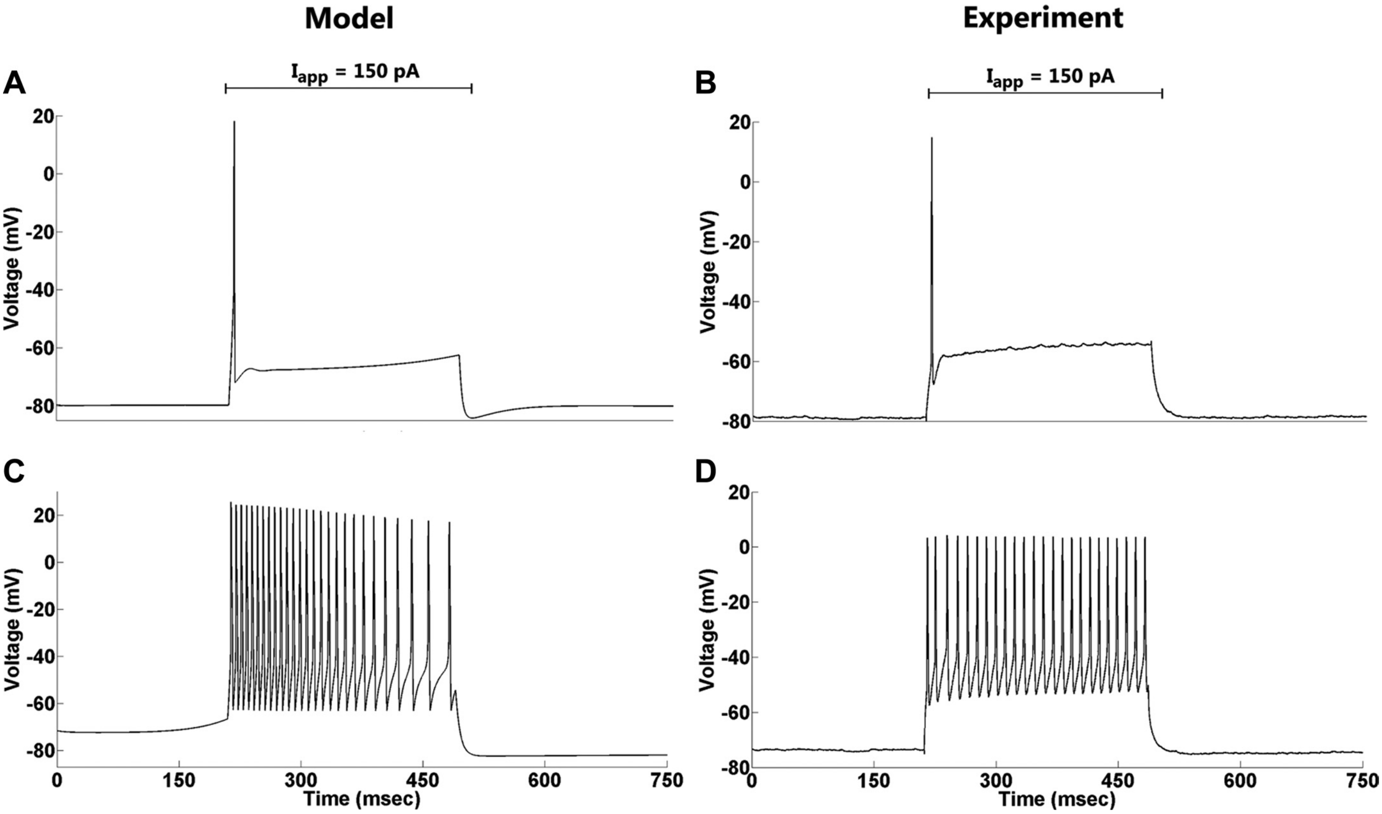

Fig. 12. Effect of I_{SK} in HVC$_{RA}$ neurons. *A*: a model HVC$_{RA}$ neuron with the same parameters as in Fig. 9*C* but with g_{KNa} = 100 nS, g_A = 0 nS, g_{SK} = 35 nS, and $g_{Ca\text{-}T}$ = 6 nS. *B*: an RA-projecting neuron exhibits a single action potential with no delay. *C*: blocking I_{SK} in the model (g_{SK} = 0) caused a dramatic increase in excitability, decreased the spike amplitude slightly, increased the resting membrane potential by ~8 mV, and exhibited adaptation due to I_{KNa}. *D*: blocking I_{SK} using apamin (150 nM) greatly increased the neuron's excitability, decreased the spike amplitude, and depolarized the resting membrane potential by ~5 mV. Unlike the model response, however, no adaptation was seen in this neuron.

g_h remains at an elevated level, contributing to the rebound firing.

Blockade of I_h is simulated in the model by setting g_h to 0. This results in a small decline in the resting membrane potential and a much larger hyperpolarization during the current pulse. This is because the resting I_h current conductance has been eliminated, so there is less I_h current to resist the hyperpolarization. The sag is gone and there is a delayed weak rebound spike, due to $I_{Ca\text{-}T}$.

Model predictions were tested and verified in the slice by pharmacologically blocking I_h using ZD 7288 (50 μM; Fig. 16*D*). ZD 7288 application eliminated the sag and the strong rebound firing, but a weak delayed rebound spike remained (Fig. 16*D*, red trace, 25 min after drug application) in the same interneuron used in Fig. 13*B*. Moreover, the resting membrane potential was hyperpolarized by ~8 mV. Similar behavior was observed in four additional HVC$_{INT}$ neurons. Therefore, the sag seen in HVC$_{INT}$ neurons is due to the hyperpolarization-activated inward current, which also contributes to rebound firing. In another four HVC$_{INT}$ neurons, mibefradil application eliminated rebound firing (not shown), confirming the existence and role of $I_{Ca\text{-}T}$ in these neurons, as well.

DISCUSSION

This study identified ionic currents present in zebra finch HVC neurons, which was facilitated by the development of computational models of the three types of HVC neurons. These models were based on current-clamp recordings reported in the literature (Dutar et al. 1998; Kubota and Saito 1991; Kubota and Taniguchi 1998; Mooney 2000; Mooney et al. 2001; Mooney and Prather 2005; Shea et al. 2010; Wild et al. 2005) and on our own current-clamp data. The calibrated models were used to generate predictions about the roles that the different ionic currents play in shaping the characteristic firing patterns of each of the HVC neurons types. The predictions were then tested and verified in the slice by varying the applied current or pharmacologically blocking ionic currents of HVC neurons. Our data identified a hyperpolarization-activated inward current (I_h) and a low-threshold T-type Ca^{2+} current ($I_{Ca\text{-}T}$) in the HVC$_X$ and HVC$_{INT}$ neurons and a Ca^{2+}-activated K$^+$ current (I_{SK}) and an A-type K$^+$ current (I_A) in the HVC$_{RA}$ neurons, as well as highlighting a possible role for the Na$^+$-dependent K$^+$ current (I_{KNa}) in the HVC$_X$ neurons. Figure 17 summarizes the conductance values presented in Tables 1 and 2 and shows a schematic of the three model HVC neurons depicting their corresponding ionic currents. The relative magnitudes of the various conductance parameters within a particular model neuron are reflected by the sizes of the corresponding cartoon ion channels (size computed based on logarithmic scale). The variation in the balance of these various ionic currents shapes the firing properties of model HVC neurons.

Previous research characterized the electrophysiological properties of the different classes of HVC neurons (Dutar et al.

Downloaded from http://jn.physiology.org/ at Florida State University on September 3, 2013

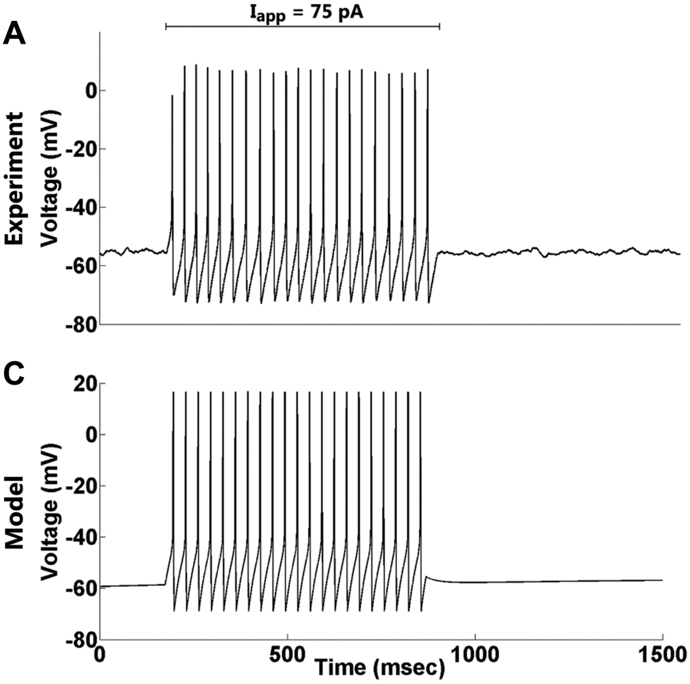

Fig. 13. Firing properties of an HVC interneuron. *A*: an HVC interneuron fires tonically at high frequencies in response to a depolarizing current pulse (75 pA). *B*: a prominent sag followed by postinhibitory rebound firing is generated in response to a hyperpolarizing current pulse (−120 pA). *C* and *D*: HVC_{INT} model neuron parameters were calibrated to match the voltage traces.

1998; Kubota and Saito 1991; Kubota and Taniguchi 1998; Mooney 2000; Schmidt and Perkel 1998; Shea et al. 2010). These properties include the resting membrane potential, input resistance, sag, spike duration, spike threshold, AHP amplitude, and AHP time to peak. Moreover, morphological characterization and visualization of HVC neurons had been performed post hoc in a few of these and other studies (Dutar et al. 1998; Kubota and Saito 1991; Kubota and Taniguchi 1998; Mooney 2000; Mooney and Prather 2005; Shea et al. 2010; Wild et al. 2005). We used this electrophysiological characterization to identify our HVC neurons and performed our own morphological studies to support this means of identification. Our electrical recordings were consistent with those of the previous studies, and our anatomically identified cells confirmed the classification of neurons on the basis of their physiological properties. A panel of intrinsic property measurements for each of the classes of HVC neurons is reported in Table 3.

Hyperpolarization-activated ionic conductances are a prevalent feature of electrically excitable cells, including frog skeletal muscle fibers, heart, photoreceptors, neurons in the peripheral and central nervous system, and some types of axons (Pape 1996). The sag we observed in HVC_X and HVC_{INT} neurons in response to hyperpolarizing current pulses was completely abolished after the application of the drug ZD 7288 in all of the neurons tested (Figs. 6, 7, and 16), indicating that the sag in these HVC neurons is due to the hyperpolarization-activated inward current (I_h). In other types of neurons, two kinetically distinct components of I_h have

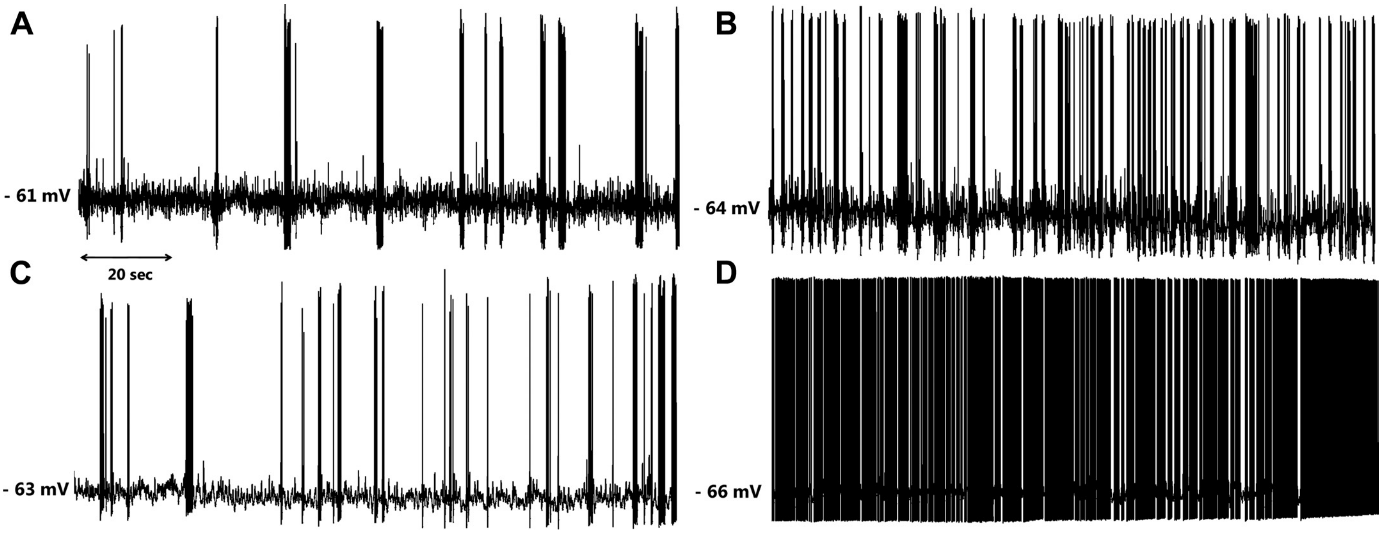

Fig. 14. Most HVC_{INT} neurons in the slice exhibited spontaneous firing (n = 18). *A*–*D*: spontaneous firing in 4 different HVC_{INT} neurons.

Downloaded from http://jn.physiology.org/ at Florida State University on September 3, 2013

Fig. 15. The firing frequency of a model $\mathrm{HVC_{INT}}$ neuron under various current injections (triangles) closely matches the data from interneurons in the slice (circles, $n = 15$). Values are means ± SE. For both model and actual $\mathrm{HVC_{INT}}$ neurons, the duration of applied current was 1 s.

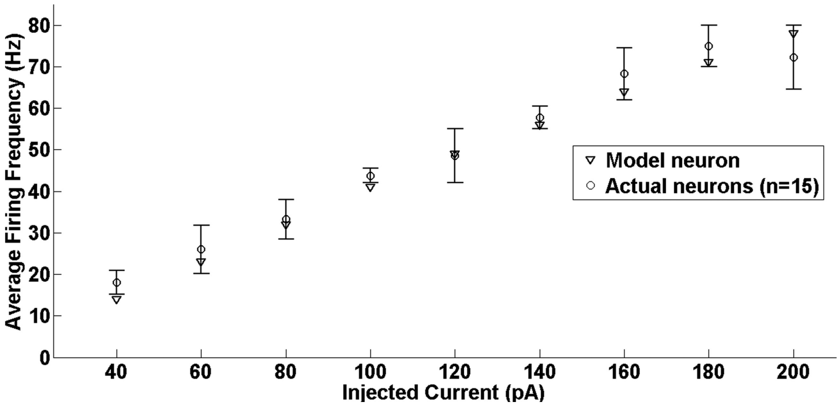

been identified with time constants in the range of hundreds of milliseconds and seconds, respectively (Banks et al. 1993; Budde et al. 1994; Solomon et al. 1993). We found that our models fit the data best when the relative strength of these components is different in the three types of HVC neurons.

The unique nature of I_h, i.e., an inward current activated on hyperpolarization beyond resting potential, makes it particularly useful in rhythmogenesis. Reported examples include *1*) rhythmic activity of the crustacean stomatogastric ganglion, where I_h in lateral pyloric neurons controls phase relationships in the pyloric network (Golowasch et al. 1992; Golowasch and Marder 1992); and *2*) slow oscillatory activity of interneurons that control heartbeat in the leech, where I_h mediates the escape from inhibition that times the phase transition of two interconnected neurons (Angstadt and Calabrese 1989). Another study done by Thoby-Brisson et al. (2000) on the respiratory rhythm generated by the pre-Botzinger complex showed that inhibiting I_h can actually increase the frequency of rhythmic activity, which is counter-intuitive and demonstrates the subtle actions of this subthreshold current. In thalamocortical neurons, the properties of the I_h current and the critical role it plays in slow thalamic oscillations have been extensively investigated (Budde et al. 1997; McCormick and Pape 1990; Munsch and Pape 1999; Pape 1996). In the HVC of songbirds, the role that I_h plays in controlling their vocal pattern remains to be investigated.

The existence of a low-voltage activated $\mathrm{Ca^{2+}}$ current in HVC neurons was first shown by Kubota and Saito (1991), and we have shown here the key role it plays in rebound spiking (Figs. 6, 7, and 13). This current is known to be important in other systems as an ionic current for burst generation (Huguenard 1996). This has been characterized in several cell types

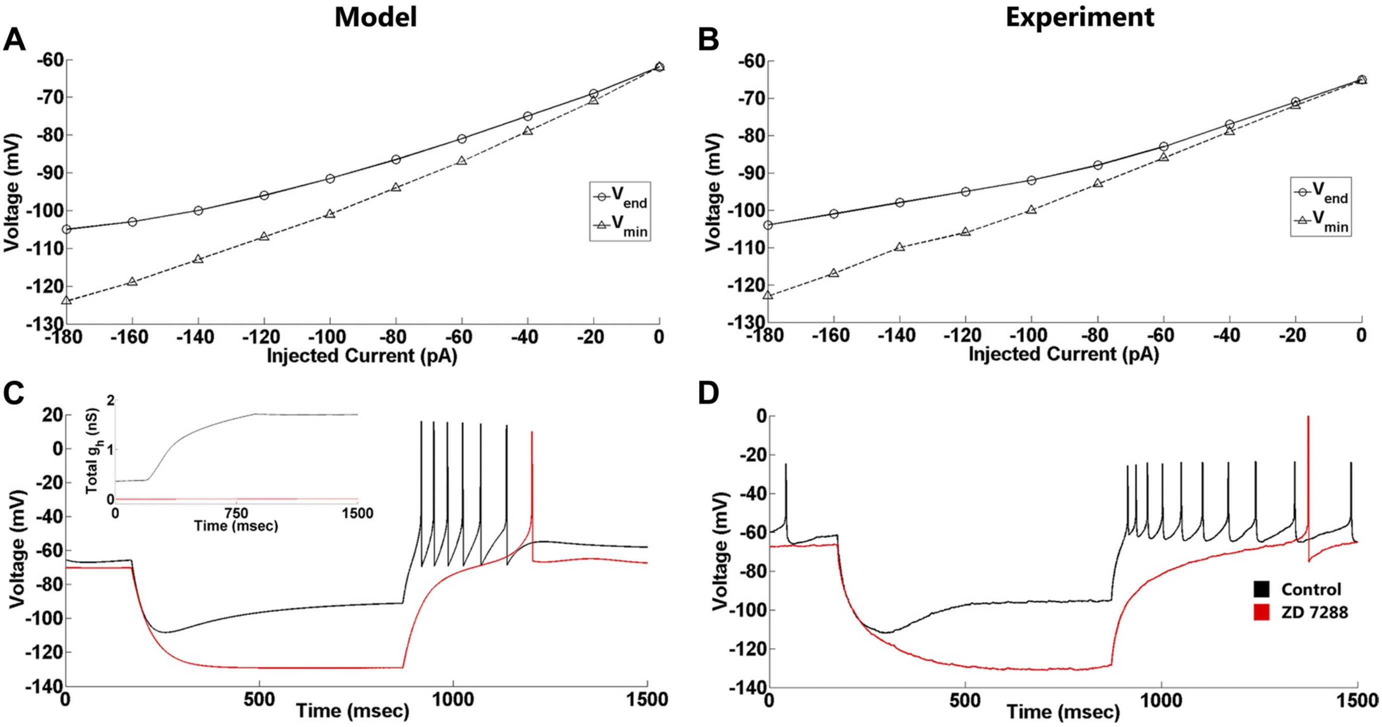

Fig. 16. Inward rectification and I_h current in $\mathrm{HVC_{INT}}$ neurons. *A*: current-voltage relationship of a model $\mathrm{HVC_{INT}}$ neuron using the same parameters as in Fig. 13. Circles with solid curve represent voltage responses measured at the end of the current pulses, whereas triangles with dashed curve represent voltage at the nadir. *B*: an HVC interneuron exhibits inward rectification over a range of currents that is captured by the model. *C*: the sag generated in the model $\mathrm{HVC_{INT}}$ neuron is due to I_h ($g_h = 4$ nS), which also contributes to the rebound (black trace). Blocking I_h by setting g_h to 0 eliminates the sag and generates a weak rebound with a long delay due to $I_{\mathrm{Ca\text{-}T}}$. *Inset* shows the total I_h conductance increasing during the negative current pulse. *D*: blocking I_h using ZD 7288 (50 μM) eliminates the sag and generates a delayed rebound (red trace, 25 min after ZD 7288 application) in the same interneuron used in Fig. 13*B*, matching model predictions.

Downloaded from http://jn.physiology.org/ at Florida State University on September 3, 2013

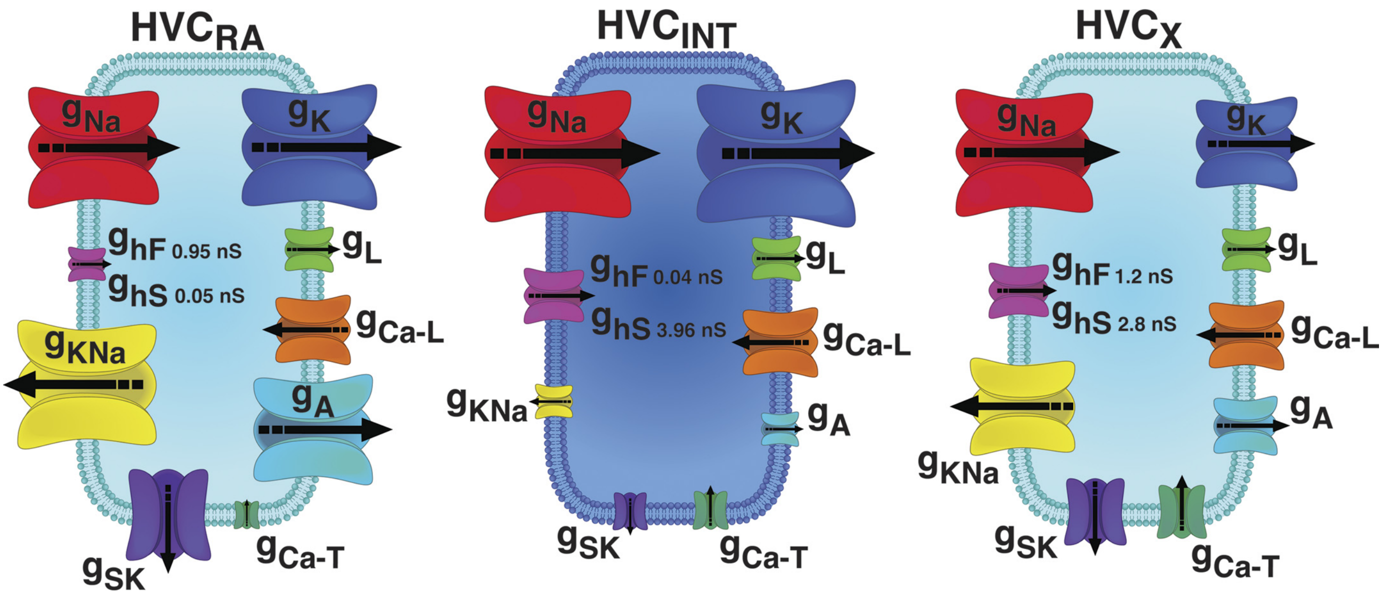

Fig. 17. Schematic models depicting the ionic currents present in each of 3 HVC model neurons after calibration to our data. Similar ionic conductances across the 3 classes of HVC neurons are coded with the same colors. The relative magnitudes of the various conductance parameters presented in Tables 1 and 2 for a particular model neuron are reflected by the sizes of the corresponding cartoon ion channels (size computed based on logarithmic scale). This shows indirectly the contributions of the various ionic currents to shaping the firing properties of the model HVC neurons. The I_h current conductance has fast (g_{hf}) and slow (g_{hs}) components.

that include thalamic reticular (Mulle et al. 1986) and relay cells (Deschenes et al. 1982; Llinas and Jahnsen 1982), inferior olive cells (Llinas and Yarom 1981a, 1981b), hippocampal interneurons (Fraser and MacVicar 1991), lateral habenular neurons (Wilcox et al. 1988), a subpopulation of pontine reticular formation cells (Gerber et al. 1989), and neocortical neurons (Friedman and Gutnick 1987). Bursting activity in HVC neurons has been reported to occur in vivo during singing (Hahnloser et al. 2002; Kozhevnikov and Fee 2007; Long et al. 2010). Moreover, Lewicki (1996) showed that auditory HVC neurons in vivo exhibit a significant hyperpolarization before emitting their bursts, and the strength of the burst is correlated with the degree of hyperpolarization. The role the T-type Ca^{2+} current plays in HVC neuron bursting in vivo has yet to be investigated.

The adaptation we observed in HVC_X neurons was unaltered by apamin application ($n = 4$). This demonstrates that SK channels are not solely responsible for adaptation in these neurons. However, apamin did decrease the AHP following each action potential, consistent with prior reports (Kubota and Saito 1991; Schmidt and Perkel 1998). Apamin also depolarized the resting membrane potential by a few millivolts in these neurons. Apamin application, however, had a dramatic effect on HVC_{RA} neurons. These neurons normally fire one or few spikes on depolarization, but when the SK current was blocked they fired throughout the duration of the depolarizing current pulse (Fig. 12). Thus SK current plays a major role in inhibiting the excitability of HVC_{RA} neurons.

We also investigated the role played by A-type K^+ channels, using the blocker 4-AP. This eliminated the delay to spiking in HVC_{RA} neurons and increased their resting membrane potential. It also reduced the AHP following each spike. Since both 4-AP and apamin increased the resting membrane potential of HVC_{RA} neurons, I_A and I_{SK} must both contribute to the extremely hyperpolarized resting membrane potential of HVC_{RA} neurons, a distinctive feature of these neurons.

The ionic currents presented here motivate speculation on the role they play from a circuit-level perspective. Evidence shows that neural activity in the HVC propagates preferentially within its rostrocaudal axis (Day et al. 2013; Stauffer et al. 2012). Moreover, Mooney and Prather (2005) identified several synaptic interactions among the three HVC neuronal subpopulations in zebra finch brain slices. These findings, combined with our models, could serve as a starting point to develop realistic and plausible neural architectures that would reflect an accurate topography of the nucleus as well as produce the characteristic patterns of neural activity exhibited by HVC_{RA}, HVC_X, and HVC_{INT} during singing. This of course requires more investigation of the connectivity patterns among the different types of HVC neurons.

The models that we developed consist of a single compartment. One could construct multicompartment models to better represent the spatial aspects of HVC neurons, although to do this well it would be necessary to first study dendritic properties of the neuron, including ion channel distribution. Also, in our model description of ionic currents, we utilized functional forms used in prior published neural modeling studies of non-HVC neurons. We did not attempt to calibrate the shape parameters of these functions, which would best be done using a voltage-clamp protocol or by using dynamical estimation methods as in Toth et al. (2011). Doing this calibration would improve the fit of the models. Finally, pharmacological blockers could be used with a range of current pulses (rather than just one depolarizing pulse and one hyperpolarizing pulse, as done here) to better constrain the model parameter values. This being said, the current models provide a large step forward in describing the biophysics of HVC neurons.

GRANTS

This work was supported by National Science Foundation Grant IOS-1146607 (to F. Johnson, R. Bertram, and R. L. Hyson).

Downloaded from http://jn.physiology.org/ at Florida State University on September 3, 2013

DISCLOSURES

No conflicts of interest, financial or otherwise, are declared by the authors.

AUTHOR CONTRIBUTIONS

A.D., F.J., R.L.H., and R.B. conception and design of research; A.D. and M.T.R. performed experiments; A.D. analyzed data; A.D., M.T.R., F.J., R.L.H., and R.B. interpreted results of experiments; A.D., M.T.R., F.J., and R.B. prepared figures; A.D. drafted manuscript; A.D., M.T.R., F.J., R.L.H., and R.B. edited and revised manuscript; A.D., M.T.R., F.J., R.L.H., and R.B. approved final version of manuscript.

REFERENCES

Abarbanel H, Talathi S, Mindlin G, Rabinovich M, Gibb L. Dynamical model of birdsong maintenance and control. *Phys Rev E Stat Nonlin Soft Matter Phys* 70: 051911, 2004a.

Abarbanel HD, Gibb L, Mindlin GB, Rabinovich MI, Talathi S. Spike timing and synaptic plasticity in the premotor pathway of birdsong. *Biol Cybern* 91: 159–167, 2004b.

Abarbanel HD, Meliza C, Kostuk M, Huang H, Margoliash D. Dynamic parameter estimation for biophysical models of HVC neurons. Program No. 712.24. *2012 Neuroscience Meeting Planner*. New Orleans, LA: Society for Neuroscience, 2012.

Aghajanian GK, Rasmussen K. Intracellular studies in the facial nucleus illustrating a simple new method for obtaining viable motoneurons in adult rat brain slices. *Synapse* 3: 331–338, 1989.

Angstadt JD, Calabrese RL. A hyperpolarization-activated inward current in heart interneurons of the medicinal leech. *J Neurosci* 9: 2846–2857, 1989.

Banks MI, Pearce RA, Smith PH. Hyperpolarization-activated cation current (I_h) in neurons of the medial nucleus of the trapezoid body: voltage-clamp analysis and enhancement by norepinephrine and cAMP suggest a modulatory mechanism in the auditory brain stem. *J Neurophysiol* 70: 1420–1432, 1993.

Bolhuis JJ, Gahr M. Neural mechanisms of birdsong memory. *Nat Rev Neurosci* 7: 347–357, 2006.

Bolhuis JJ, Okanoya K, Scharff C. Twitter evolution: converging mechanisms in birdsong and human speech. *Nat Rev Neurosci* 11: 747–759, 2010.

Bottjer SW, Arnold AP. Developmental plasticity in neural circuits for a learned behavior. *Annu Rev Neurosci* 20: 459–481, 1997.

Brainard MS, Doupe AJ. Auditory feedback in learning and maintenance of vocal behaviour. *Nat Rev Neurosci* 1: 31–40, 2000.

Brainard MS, Doupe AJ. What songbirds teach us about learning. *Nature* 417: 351–358, 2002.

Budde T, Biella G, Munsch T, Pape HC. Lack of regulation by intracellular Ca^{2+} of the hyperpolarization-activated cation current in rat thalamic neurones. *J Physiol* 503: 79–85, 1997.

Budde T, White JA, Kay AR. Hyperpolarization-activated Na^+-K^+ current (I_h) in neocortical neurons is blocked by external proteolysis and internal TEA. *J Neurophysiol* 72: 2737–2742, 1994.

Day NF, Terleski KL, Nykamp DQ, Nick TA. Directed functional connectivity matures with motor learning in a cortical pattern generator. *J Neurophysiol* 109: 913–923, 2013.

Deschenes M, Roy JP, Steriade M. Thalamic bursting mechanism: an inward slow current revealed by membrane hyperpolarization. *Brain Res* 239: 289–293, 1982.

Destexhe A, Babloyantz A. A model of the inward current Ih and its possible role in thalamocortical oscillations. *Neuroreport* 4: 223–226, 1993.

Doupe A, Perkel D, Reiner A, Stern E. Birdbrains could teach basal ganglia research a new song. *Trends Neurosci* 28: 353–363, 2005.

Drew PJ, Abbott LF. Model of song selectivity and sequence generation in area HVc of the songbird. *J Neurophysiol* 89: 2697–2706, 2003.

Dunmyre JR, Del Negro CA, Rubin JE. Interactions of persistent sodium and calcium-activated nonspecific cationic currents yield dynamically distinct bursting regimes in a model of respiratory neurons. *J Comput Neurosci* 31: 305–328, 2011.

Dutar P, Vu HM, Perkel DJ. Multiple cell types distinguished by physiological, pharmacological, and anatomic properties in nucleus HVC of the adult zebra finch. *J Neurophysiol* 80: 1828–1838, 1998.

Fain G. *Molecular and Cellular Physiology of Neurons*. Cambridge, MA: Harvard University Press, 1999.

Fee MS, Goldberg JH. A hypothesis for basal ganglia-dependent reinforcement learning in the songbird. *Neuroscience* 198: 152–170, 2011.

Fee MS, Kozhevnikov AA, Hahnloser RH. Neural mechanisms of vocal sequence generation in the songbird. *Ann NY Acad Sci* 1016: 153–170, 2004.

Fee MS, Scharff C. The songbird as a model for the generation and learning of complex sequential behaviors. *ILAR J* 51: 362–377, 2010.

Fraser DD, MacVicar BA. Low-threshold transient calcium current in rat hippocampal lacunosum-moleculare interneurons: kinetics and modulation by neurotransmitters. *J Neurosci* 11: 2812–2820, 1991.

Friedman A, Gutnick MJ. Low-threshold calcium electrogenesis in neocortical neurons. *Neurosci Lett* 81: 117–122, 1987.

Gerber U, Greene RW, McCarley RW. Repetitive firing properties of medial pontine reticular formation neurones of the rat recorded in vitro. *J Physiol* 410: 533–560, 1989.

Gibb L, Gentner TQ, Abarbanel HD. Brain stem feedback in a computational model of birdsong sequencing. *J Neurophysiol* 102: 1763–1778, 2009a.

Gibb L, Gentner TQ, Abarbanel HDI. Inhibition and recurrent excitation in a computational model of sparse bursting in song nucleus HVC. *J Neurophysiol* 102: 1748–1762, 2009b.

Golowasch J, Buchholtz F, Epstein IR, Marder E. Contribution of individual ionic currents to activity of a model stomatogastric ganglion neuron. *J Neurophysiol* 67: 341–349, 1992.

Golowasch J, Marder E. Ionic currents of the lateral pyloric neuron of the stomatogastric ganglion of the crab. *J Neurophysiol* 67: 318–331, 1992.

Hahnloser RH, Kozhevnikov AA, Fee MS. An ultra-sparse code underlies the generation of neural sequences in a songbird. *Nature* 419: 65–70, 2002.

Hodgkin AL, Huxley AF. A quantitative description of membrane current and its application to conduction and excitation in nerve. *J Physiol* 117: 500–544, 1952.

Huguenard JR. Low-threshold calcium currents in central nervous system neurons. *Annu Rev Physiol* 58: 329–348, 1996.

Jaffe DB, Johnston D, Lasser-Ross N, Lisman JE, Miyakawa H, Ross WN. The spread of Na^+ spikes determines the pattern of dendritic Ca^{2+} entry into hippocampal neurons. *Nature* 357: 244–246, 1992.

Jin DZ. Generating variable birdsong syllable sequences with branching chain networks in avian premotor nucleus HVC. *Phys Rev E Stat Nonlin Soft Matter Phys* 80: 051902, 2009.

Jin DZ, Ramazanoglu FM, Seung HS. Intrinsic bursting enhances the robustness of a neural network model of sequence generation by avian brain area HVC. *J Comput Neurosci* 23: 283–299, 2007.

Katahira K, Okanoya K, Okada M. A neural network model for generating complex birdsong syntax. *Biol Cybern* 97: 441–448, 2007.

Katz LC, Gurney ME. Auditory responses in the zebra finch's motor system for song. *Brain Res* 221: 192–197, 1981.

Kozhevnikov AA, Fee MS. Singing-related activity of identified HVC neurons in the zebra finch. *J Neurophysiol* 97: 4271–4283, 2007.

Kubota M, Saito N. Sodium- and calcium-dependent conductances of neurones in the zebra finch hyperstriatum ventrale pars caudale in vitro. *J Physiol* 440: 131–142, 1991.

Kubota M, Taniguchi I. Electrophysiological characteristics of classes of neuron in the HVC of the zebra finch. *J Neurophysiol* 80: 914–923, 1998.

Lacinova L. Pharmacology of recombinant low-voltage activated calcium channels. *Curr Drug Targets CNS Neurol Disord* 3: 105–111, 2004.

Lacinova L. Voltage-dependent calcium channels. *Gen Physiol Biophys* 24, *Suppl* 1: 1–78, 2005.

Lewicki MS. Intracellular characterization of song-specific neurons in the zebra finch auditory forebrain. *J Neurosci* 16: 5855–5863, 1996.

Lewicki MS, Konishi M. Mechanisms underlying the sensitivity of songbird forebrain neurons to temporal order. *Proc Natl Acad Sci USA* 92: 5582–5586, 1995.

Li M, Greenside H. Stable propagation of a burst through a one-dimensional homogeneous excitatory chain model of songbird nucleus HVC. *Phys Rev E Stat Nonlin Soft Matter Phys* 74: 011918, 2006.

Li YX, Bertram R, Rinzel J. Modeling *N*-methyl-D-aspartate-induced bursting in dopamine neurons. *Neuroscience* 71: 397–410, 1996.

Llinas R, Jahnsen H. Electrophysiology of mammalian thalamic neurones in vitro. *Nature* 297: 406–408, 1982.

Llinas R, Yarom Y. Electrophysiology of mammalian inferior olivary neurones in vitro. Different types of voltage-dependent ionic conductances. *J Physiol* 315: 549–567, 1981a.

Llinas R, Yarom Y. Properties and distribution of ionic conductances generating electroresponsiveness of mammalian inferior olivary neurones in vitro. *J Physiol* 315: 569–584, 1981b.

Long MA, Fee MS. Using temperature to analyse temporal dynamics in the songbird motor pathway. *Nature* 456: 189–194, 2008.

Downloaded from http://jn.physiology.org/ at Florida State University on September 3, 2013

Long MA, Jin DZ, Fee MS. Support for a synaptic chain model of neuronal sequence generation. *Nature* 468: 394–399, 2010.

Margoliash D. Sleep, learning, birdsong. *ILAR J* 51: 378–386, 2010.

Margoliash D, Schmidt MF. Sleep, off-line processing, and vocal learning. *Brain Lang* 115: 45–58, 2010.

McCormick DA, Pape HC. Properties of a hyperpolarization-activated cation current and its role in rhythmic oscillation in thalamic relay neurones. *J Physiol* 431: 291–318, 1990.

Mooney R. Different subthreshold mechanisms underlie song selectivity in identified HVc neurons of the zebra finch. *J Neurosci* 20: 5420–5436, 2000.

Mooney R. Neural mechanisms for learned birdsong. *Learn Mem* 16: 655–669, 2009.

Mooney R, Hoese W, Nowicki S. Auditory representation of the vocal repertoire in a songbird with multiple song types. *Proc Natl Acad Sci USA* 98: 12778–12783, 2001.

Mooney R, Prather JF. The HVC microcircuit: the synaptic basis for interactions between song motor and vocal plasticity pathways. *J Neurosci* 25: 1952–1964, 2005.

Mooney R, Spiro JE. Bird song: of tone and tempo in the telencephalon. *Curr Biol* 7: R289–291, 1997.

Mulle C, Madariaga A, Deschenes M. Morphology and electrophysiological properties of reticularis thalami neurons in cat: in vivo study of a thalamic pacemaker. *J Neurosci* 6: 2134–2145, 1986.

Munsch T, Pape HC. Modulation of the hyperpolarization-activated cation current of rat thalamic relay neurones by intracellular pH. *J Physiol* 519: 493–504, 1999.

Nottebohm F. The neural basis of birdsong. *PLoS Biol* 3: e164, 2005.

Pape HC. Queer current and pacemaker: the hyperpolarization-activated cation current in neurons. *Annu Rev Physiol* 58: 299–327, 1996.

Rose CR, Kovalchuk Y, Eilers J, Konnerth A. Two-photon Na^+ imaging in spines and fine dendrites of central neurons. *Pflügers Arch* 439: 201–207, 1999.

Rose CR, Ransom BR. Regulation of intracellular sodium in cultured rat hippocampal neurones. *J Physiol* 499: 573–587, 1997.

Schmidt MF, Perkel DJ. Slow synaptic inhibition in nucleus HVC of the adult zebra finch. *J Neurosci* 18: 895–904, 1998.

Shea SD, Koch H, Baleckaitis D, Ramirez JM, Margoliash D. Neuron-specific cholinergic modulation of a forebrain song control nucleus. *J Neurophysiol* 103: 733–745, 2010.

Simonyan K, Horwitz B, Jarvis ED. Dopamine regulation of human speech and bird song: a critical review. *Brain Lang* 122: 142–150, 2012.

Solis MM, Perkel D. Rhythmic activity in a forebrain vocal control nucleus in vitro. *J Neurosci* 25: 2811–2822, 2005.

Solomon JS, Doyle JF, Burkhalter A, Nerbonne JM. Differential expression of hyperpolarization-activated currents reveals distinct classes of visual cortical projection neurons. *J Neurosci* 13: 5082–5091, 1993.

Stauffer TR, Elliott KC, Ross MT, Basista MJ, Hyson RL, Johnson F. Axial organization of a brain region that sequences a learned pattern of behavior. *J Neurosci* 32: 9312–9322, 2012.

Terman D, Rubin JE, Yew AC, Wilson CJ. Activity patterns in a model for the subthalamopallidal network of the basal ganglia. *J Neurosci* 22: 2963–2976, 2002.

Thoby-Brisson M, Telgkamp P, Ramirez JM. The role of the hyperpolarization-activated current in modulating rhythmic activity in the isolated respiratory network of mice. *J Neurosci* 20: 2994–3005, 2000.

Toth BA, Kostuk M, Meliza CD, Margoliash D, Abarbanel HD. Dynamical estimation of neuron and network properties. I: variational methods. *Biol Cybern* 105: 217–237, 2011.

Troyer TW, Doupe AJ. An associational model of birdsong sensorimotor learning. II. Temporal hierarchies and the learning of song sequence. *J Neurophysiol* 84: 1224–1239, 2000.

Vu ET, Mazurek ME, Kuo YC. Identification of a forebrain motor programming network for the learned song of zebra finches. *J Neurosci* 14: 6924–6934, 1994.

Wang XJ, Liu Y, Sanchez-Vives MV, McCormick DA. Adaptation and temporal decorrelation by single neurons in the primary visual cortex. *J Neurophysiol* 89: 3279–3293, 2003.

Wilcox KS, Gutnick MJ, Christoph GR. Electrophysiological properties of neurons in the lateral habenula nucleus: an in vitro study. *J Neurophysiol* 59: 212–225, 1988.

Wild JM, Williams MN, Howie GJ, Mooney R. Calcium-binding proteins define interneurons in HVC of the zebra finch (*Taeniopygia guttata*). *J Comp Neurol* 483: 76–90, 2005.

Williams H. Birdsong and singing behavior. *Ann NY Acad Sci* 1016: 1–30, 2004.

Yu AC, Margoliash D. Temporal hierarchical control of singing in birds. *Science* 273: 1871–1875, 1996.

Downloaded from http://jn.physiology.org/ at Florida State University on September 3, 2013